Human mitochondrial DNA variants influence telomere length: evidence from a transmitochondrial cybrid model

Manon Mahieu[1,#], Jean-Philippe Defour[2,3,#], Barbara Mathieu[4], Elena Richiardone[5], Isaac Heremans[6], Gabriel Levy[2], Gabriel Le Berre[1], Isabelle Scheers[2], Bénédicte Brichard[2], Thierry Arnould[7], Guido Bommer[6], Bernard Gallez[4], Cyril Corbet[5,*] & Anabelle Decottignies[1,*]

[1] Genetic & Epigenetic Alterations of Genomes, de Duve Institute, UCLouvain, Brussels, Belgium

[2] Cliniques Universitaires Saint-Luc, UCLouvain, Brussels, Belgium

[3] Current address: CHC Liège, Liège, Belgium

[4] Biomedical Magnetic Resonance Unit, Louvain Drug Research Institute, UCLouvain, 1200 Brussels, Belgium

[5] Pole of Pharmacology and Therapeutics, Institut de Recherche Expérimentale et Clinique, UCLouvain, Brussels, Belgium

[6] Biochemistry, de Duve Institute, UCLouvain, Brussels, Belgium

[7] Laboratory of Biochemistry and Cell Biology, NAmur Research Institute for LIfe Sciences (NARILIS), UNamur, Namur, Belgium

# These authors contributed equally

[*] Corresponding authors: anabelle.decottignies@uclouvain.be, cyril.corbet@uclouvain.be

Running title: Mitochondrial genome impacts telomere length

Abstract

Telomere shortening is a hallmark of aging, yet telomere length (TL) varies considerably among individuals and is strongly influenced by inheritance. In mice, efficient mitochondrial function—characterized by low reactive oxygen species (ROS) production—is critical for telomere elongation during early embryogenesis. Since mitochondrial DNA (mtDNA) encodes several subunits of the electron transport chain, it may influence TL at birth by regulating mitochondrial function *in utero*. To explore the relationship between mtDNA and TL, we used a transmitochondrial cybrid approach, introducing mitochondria from donor platelets with varying TLs into mtDNA-depleted cells. This revealed an inverse correlation between donor blood TL and mitochondrial ROS levels in the resulting cybrids. Under the specific experimental conditions of cybrid formation, characterized by a metabolic shift from glycolysis to oxidative phosphorylation, mtDNA variants linked to lower complex I activity triggered rapid telomere shortening, further implicating mitochondrial metabolism in TL regulation. Notably, this effect was prevented by antioxidant treatment and NAD^+ precursor supplementation. Collectively, these findings establish a connection between the mitochondrial genome and human TL, and highlight the pivotal role of complex I in supporting NAD^+ metabolism and preserving telomere integrity under oxidative stress.

Keywords: Mitochondrial genome, Telomeres, Telomere length inheritance, Oxidative stress, Complex I, Transmitochondrial cybrid

Introduction

Telomeres form protective caps at chromosome ends thanks to the binding of a six-member protein complex termed shelterin (de Lange 2018). With cell divisions, telomeres of normal somatic cells progressively shorten, a process that likely contributes to cellular aging and the development of various age-related pathologies (Campisi et al. 2011; López-Otín et al. 2023). Accordingly, cohort studies established that shorter leucocyte telomere length (TL) was associated with a higher risk of diseases affecting specific organs, such as the lung or the liver, and an increased incidence of esophageal cancer, as well as lymphoid and myeloid leukemia (Schneider et al. 2022).

While aging is a key determinant of TL, genetic variation also plays a significant role in the variability of leukocyte TL among healthy individuals, as evidenced by the identification of nuclear genomic SNPs associated with TL (Demanelis et al. 2020). Heritability estimates for human TL reach 82% (Broer et al. 2013). Consistently, TL in the zygote appears to play a key role in determining TL later in life (Demanelis et al. 2020), indicating that it is largely established during early embryonic development. Telomere length resetting during embryogenesis is a telomerase-dependent process that occurs at the morula-to-blastocyst transition (Schaetzlein et al. 2004). Recent findings in mice show that experimentally disrupting mitochondrial function in zygotes significantly impairs telomere elongation between the 8-cell and blastocyst stages, ultimately leading to shorter telomeres in the offspring (Winstanley et al. 2025). Similar outcomes have been observed in offspring from reproductively aged or obese female mice—two conditions known to compromise oocyte mitochondrial integrity (Winstanley et al. 2025). Collectively, these findings underscore the critical role of proper mitochondrial function in telomere regulation during embryogenesis. Further evidence

comes from individuals with mitochondrial disorders such as MELAS syndrome and Leber's hereditary optic neuropathy (LHON). These individuals exhibit significantly shorter leukocyte telomeres at birth, likely reflecting impaired TL establishment during early development (Oexle and Zwirner 1997).

While damaged mitochondria are associated with shorter TL in mouse embryos and may impair TL regulation in patients with mitochondrial diseases, the impact of naturally occurring mitochondrial genome SNPs on TL remains largely unexplored. With a total of 29 haplogroups and a myriad of subhaplogroups characterized by distinct variants compiled in the Mitomap database (Ruiz-Pesini et al. 2007), human mtDNA genomes display large heterogeneity. Some variants within the coding regions of mtDNA, such as the NADH dehydrogenase subunits (ND1, 2, 3, 4, 4L and 5) of complex I (CI), Cytochrome b, the COXI, II and III subunits of CIV or the ATP6 and 8 subunits of the ATP synthase (CV) lead to distinct ETC properties that impact mitochondrial metabolism and ROS production. In line with the hypothesis that the mitochondrial genome may contribute to the observed stronger maternal influence on TL at birth (Broer et al. 2013; Nersisyan et al. 2019) —given that mtDNA is maternally inherited—, we hypothesized that non-pathogenic variation in the mtDNA sequence could affect TL.

Here, building on reference curves for TL in the Belgian population, obtained through fluorescence *in situ* hybridization (FISH) combined with flow cytometry (Flow-FISH), we identified mtDNA variants associated with either very long or short leukocyte TL. We leveraged a transmitochondrial cybrid approach to directly test the effects of these mtDNA variants on mitochondrial function in mtDNA-depleted recipient cells and uncovered an inverse relationship between leukocyte TL in the donors and mitochondrial ROS levels measured in the cybrids. Our results further highlight the

critical role of mtDNA-encoded CI activity in sustaining NAD^+ metabolism and telomere integrity, particularly under oxidative stress conditions arising during the metabolic transition from glycolysis to oxidative phosphorylation in early cybrid development. Collectively, these findings reinforce the link between mitochondrial function and telomere regulation in human cells.

Results

Establishment of reference curves for TL using Flow-FISH

To establish reference curves for TL in Belgium, we applied the gold standard Flow-FISH approach (Baerlocher et al. 2006) on leukocytes isolated from a cohort of 491 healthy donors aged 7 days to 99 years old. Percentile curves for TL in lymphocytes (Fig 1A) and granulocytes (Fig 1B) were comparable to those obtained previously (Alder et al. 2008; Aubert et al. 2012) and showed large heterogeneity among individuals of similar age (Fig 1C). Although still controversial, obesity may negatively impact TL (Demanelis et al. 2020; Mundstock et al. 2015). In our cohort, average BMI was not statistically different between donors with telomeres below the 5^{th} or above the 90^{th} percentile (Fig S1). The large variabilities in TL in our cohort were not either explained by gender nor smoking status, consistent with the idea that heritability of TL is more important than the influence of either sex or environmental cues (Demanelis et al. 2020).

Rare mtDNA variants in donors with long telomeres

Given previous evidence supporting a stronger maternal inheritance of TL in humans (Broer et al. 2013; Nersisyan et al. 2019), with similar trend observed in birds (Asghar et al. 2015), we set to investigate the potential role of the human mitochondrial

genome in TL regulation. To this end, we selected individuals with long (Long1-3), average (Aver1-2) or short (Short1-2) telomeres from our Flow-FISH curves (Fig 2A). All were of European origin, thus excluding a possible bias linked to African ethnic groups (Demanelis et al. 2020), and the seven donors belonged to distinct mitochondrial subhaplogroups (Fig 2B). Strikingly, Long3 donor, with telomeres at the 95th percentile, turned out to belong to the K1a subhaplogroup that encompasses the centenarian-enriched A177T variant (m.G9055>A) in the ATP6 subunit of ATP synthase (CV) (Ivanova et al. 1998; Ross et al. 2001) with an allele frequency of 5.4% in Mitomap database (Fig 2B). Identified by the MitoAging project as one of the four mtDNA variants significantly associated with longevity, the A177T variant also shows protective effect against Parkinson's disease (Castaneda et al. 2022). Although we could not assess TL in Long3's progeny, as she does not have children, the fact that her mother showed telomeres at the 90th percentile and that two European male donors, identified in independent cohorts (Froidure et al. 2020) as having telomeres at, respectively, the 97.5th and above the 99th percentile (Fig 2C), were found to display K1a mtDNA, support the notion that this subhaplogroup is associated with long telomere inheritance. This led us to screen additional unrelated donors with varying TL for the presence of the m.G9055>A variant. The variant was identified in 1 of 11 donors with lymphocyte TL below the 50th percentile, 2 of 26 donors with TL between the 50th and 90th percentiles, and 3 of 13 donors with TL at or above the 90th percentile (Fig 2D and S2), suggesting a trend toward higher frequency of the m.G9055>A (ATP6 A177T) variant among individuals with lymphocyte TL at or above the 90th percentile (p=0.153).

The Long1 donor does not belong to the K1a haplogroup; nevertheless, both her mother and her daughter exhibited telomere lengths at the 95th and near the 90th percentile, respectively (Fig 2C). In contrast, the telomere lengths of her husband

(hereafter referred to as Short2) and her father were slightly above the 10th and around the 50th percentile, respectively (Fig 2C). These findings pointed to a maternal inheritance pattern associated with the H1b1e mtDNA subhaplogroup, identified through blood sequencing in these women but not previously linked to longevity. While the causal link between the rare m.A3796>G variant in Long1 (ND1 T164A, CI) and the long telomere phenotype remains to be determined, this variant was absent in all 49 unrelated donors with varying telomere lengths that we screened.

Collectively, these findings support the idea that multiple mitochondrial genome SNPs may contribute to the inheritance of telomere length.

Lymphocyte TL inversely correlates with ROS levels in transmitochondrial cybrids

In mice, impaired mitochondrial function in oocytes adversely affects the telomere elongation that typically occurs between the 8-cell and blastocyst stages (Winstanley et al. 2025). Regardless of the underlying cause, this mitochondrial dysfunction was consistently associated with elevated mitochondrial ROS production (Winstanley et al. 2025).

To assess whether the mitochondrial genome of donors with long, average, or short telomeres is linked to differences in mitochondrial fitness, we measured ROS levels in transmitochondrial cybrids generated by fusing platelets from seven selected donors with mtDNA-depleted, telomerase-positive 143B Rho^0 osteosarcoma cells. Transmitochondrial cybrids receive the donors' mitochondria but no other genetic information (King and Attardi, 1989), allowing to specifically assess the impact of the mitochondrial genome. The presence of variants in cybrids was checked by sequencing and mtDNA content was evaluated by qPCR (Fig S3). Mitochondrial

superoxide production, measured by electron paramagnetic resonance (d'Hose et al. 2021) in clones #1 of all cybrids with similar mtDNA content, was lower in cybrids from Long1 to 3 donors with long telomeres as compared to donors with average or short telomeres (Fig 3A and S4A). This was not linked to distinct changes in oxidative *vs* glycolytic metabolism in the cybrids that were characterized by similar lactate/glucose and ATP/ADP ratios (Fig S4B-C). Strikingly, ROS levels in the cybrids inversely correlated with the age-adjusted TL measured by Flow-FISH in the corresponding donors' lymphocytes (Fig 3B). Elevated levels of ROS were notably detected in Short1 cybrid. The Short1 mtDNA harbors the extremely rare F63L variant (m.T6090>C; Mitomap frequency: 0.002%) in the COX1 subunit, located within a transmembrane helix in close proximity to the heme A group and associated with reduced CIV efficiency (Fig 3C-D).

Together, these findings support a role for mitochondrial function in TL regulation *in vivo*.

Low complex I activity shortens the telomeres of Rho^0 recipient cells

When mitochondria are replenished in Rho^0 cells during the formation of transmitochondrial cybrids, a shift from glycolysis to OXPHOS occurs. This shift parallels the metabolic reprogramming that occurs in the pre-implantation embryo (Hashimoto et al. 2017; Deluao et al. 2022), a process also linked to the telomerase-dependent telomere elongation phase responsible for resetting TL (Schaetzlein et al. 2004). Analysis of TL during the formation of cybrids may thus provide critical insights into the impact of maternal mtDNA on the telomeres of zygotic chromosomes by recapitulating this metabolic switch.

We therefore assessed the impact of platelet-derived mitochondria on TL in recipient cells during the early passages following cybrid selection. Remarkably, similar to the telomerase-dependent telomere elongation at the morula-to-blastocyst transition (Schaetzlein et al. 2004), fusion with platelets from Long1 and Long3 donors consistently led to telomere elongation in 143B Rho^0 recipient cells across all four initially tested cybrid clones (Fig 4A). This effect was further validated by analyzing three additional clones and comparing them to seven subclones of the parental 143B Rho^0 cells (Fig S5A). Telomere elongation was accompanied by a decreased frequency of short telomeres, as measured by TeSLA in the early passages of the cybrids (after 3-4 population doublings, PDs) (Fig 4B). Long1 cybrids—and to a lesser extent, Long3 cybrids—maintained long telomeres even after 66–68 PDs (Fig S5B).

In contrast, platelets from Long2 and Aver2 donors drastically and consistently shortened the telomeres of Rho^0 recipient cells after fusion (Fig 4A-B), a phenomenon associated with strong telomeric damages and telomere fusions in the cybrids (Fig 4C-D). Notably, telomeres in the leukocytes of Long2 and Aver2 donors were not short (Fig 2A), suggesting that the observed telomere attrition in cybrids may stem from incompatibilities between the mtDNA-encoded ETC subunits and the metabolic demands of cybrid cancer cells undergoing a shift from glycolysis to OXPHOS before full metabolic adaptation. CI plays a crucial role in regulating the NAD^+/NADH balance and this is crucial for the activity of NAD^+-dependent poly (ADP-ribose) polymerase 1) (PARP1) repair enzyme, an enzyme required for the repair of telomeres undergoing oxidative stress in cultured cells (Belenky et al. 2007; Barnes et al. 2019; Fouquerel et al. 2019). We thus hypothesized that optimal levels of CI activity may be required for telomere protection in cells experiencing acute oxidative stress during the *in vitro* metabolic shift before cellular adaptation. Consistent with this, we found significantly

lower CI activity in Long2 and Aver2 cybrids (Fig 4E) and a strong positive correlation between TL measured in the cybrids at the first passages and CI activity (Fig 4F). Supporting a lower CI activity in Long2 and Aver2 cybrids, we noticed a significant up-regulation of the NAD^+ salvage pathway genes *NAMPT* and *NAPRT1*, likely reflecting a compensatory mechanism (Fig 4G). Intriguingly, telomeres from Long2 and Aver2 cybrids progressively re-elongated in culture while cellular proliferation rate resumed (Fig S5C-E).

Long2 mtDNA displays one rare non-silent variant in the ND2 subunit of CI (m.A4917G, 5.8% frequency) while Aver2 shows two rare silent changes, in ND4 (m.C11788T, 0.1% frequency) and ND5 (m.T12696C, 0.3% frequency) subunits, but it remains to be established whether these variants are responsible for the low CI activity.

Antioxidant and NAD^+ precursor supplementation prevents telomere shortening in cybrids with low CI activity

Building on the idea that, in the context of lower CI activity, telomeres may not be able to resist oxidative stress-induced shortening, we repeated the fusion of Aver2 platelets to 143B Rho^0 cells in the presence of N-acetyl-L-cysteine (NAC) antioxidant and/or nicotinamide riboside (NR), a precursor of NAD^+. Strikingly, while telomeres were shortened in all clones (5/5) selected from cybrids obtained in the presence of N-acetyl-L-alanine (NAA) used as control, only one out of the eight selected cybrids obtained in the presence of both NAC and NR showed telomere shortening (Fig 5A-B). Treatment with either NAC or NR alone showed intermediate phenotype (Fig 5A-B). The detection of telomeric parylation signals further supported a role for NAD^+-dependent PARP1 activity in repairing oxidative damage at shortened telomeres during the process of cybrid formation (Fig 5C).

Altogether, we propose that the *in vitro* process of cybrid formation exacerbates the impact of low CI activity on telomeres during the acute oxidative stress linked to a metabolic shift from glycolysis to OXPHOS.

Discussion

While long telomeres are often viewed as markers of good cellular health, shorter leukocyte TL is linked to a higher risk of diseases affecting organs like the lungs and liver, as well as various cancers (Schneider et al. 2022). Although aging is a major factor influencing TL, genetic variation also plays a key role and helps explain why TL established in the zygote strongly influences TL throughout life (Demanelis et al. 2020). Unraveling the mechanisms that determine TL in the zygote is therefore highly relevant, particularly for optimizing *in vitro* fertilization strategies. A recent study in mice suggests that mitochondrial dysfunction impairs telomere elongation during embryonic development—a defect that was largely reversed by antioxidant treatment, highlighting the harmful effect of ROS on TL regulation in the embryo (Winstanley et al. 2025). In humans, prenatal exposure to psychological stress has also been linked to shorter leukocyte TL in offspring (Entringer et al. 2011). Given the established connection between psychological and oxidative stress (Salim 2014; Rzasa et al. 2021), these findings point to a similar influence of mitochondrial function on TL regulation during human embryogenesis. Building on these findings—and previous evidence suggesting stronger maternal inheritance of TL in humans (Broer et al. 2013; Nersisyan et al. 2019)—we hypothesized that the mitochondrial genome may influence human TL. To investigate this, we employed a transmitochondrial cybrid model using platelets from seven donors with known leukocyte TL and distinct mitochondrial subhaplogroups.

Notably, we observed an inverse correlation between donor leukocyte TL and mitochondrial ROS levels in the cybrids, indicating that mitochondrial subhaplogroup affects mitochondrial function and suggesting a potential role for mtDNA variation in shaping leukocyte TL *in vivo*.

Experimentally induced mitochondrial dysfunction leads to telomere damage (Qian et al. 2019). Mechanistically, the *TTAGGG* repeats of telomeres are exquisitely sensitive to 8-oxo-guanine formation, a lesion recognized by the base excision repair pathway that, after removal of the oxidized base, generates single-strand breaks eventually recruiting NAD+-dependent PARP1 repair enzyme (Barnes et al. 2019; Passos et al. 2007). If left unrepaired in replicating cancer cells, these breaks can convert into double-strand breaks, resulting in distal telomere loss and chromosomal fusions (Fouquerel et al. 2019). In normal fibroblasts and epithelial cells, telomeric 8-oxoG lesions induced by a chemoptogenetic tool were sufficient to activate p53-dependent senescence (Barnes et al. 2022), highlighting the harmful effects of oxidative stress at telomeres on cellular function. During the generation of transmitochondrial cybrids, cells undergo a metabolic shift from glycolysis to OXPHOS, accompanied by increased ROS production. Before cells adapt to this shift, oxidative stress can be particularly damaging. Supporting the essential role of CI in maintaining PARP1 activity *via* regulation of the NAD^+/NADH balance, mitochondrial platelets with low CI activity triggered significant telomere shortening in recipient cells during early cybrid formation—a loss that was prevented by co-treatment with an antioxidant and an NAD^+ precursor. Although the observed telomere loss may be exacerbated by the *in vitro* oxidative stress conditions—since donors with low CI activity did not show short leukocyte telomeres—our findings are consistent with reports that NAD^+ supplementation can alleviate telomere dysfunction in cells from dyskeratosis

congenita patients (Sun et al. 2020) and improve hematopoietic function and telomere integrity in Tert$^{-/-}$ mice (Stock et al. 2023). Data are also consistent with the observation that mice lacking PARP display telomere shortening and chromosomal instability (d'Adda di Fagagna et al. 1999) and that NAD^+ repletion rescues fertility of aging female mice (Bertoldo et al. 2020). Together, these data bring support to the hypothesis that, when extremely pathogenic and associated with high oxidative stress levels, such as in MELAS or LHON patients (Zhuo et al. 2012), mutations in CI may impair telomere length resetting *in utero*.

Mitochondrial ROS are generally considered harmful to telomeres. Yet, the finding that telomerase-dependent telomere elongation at the morula-to-blastocyst stage in mouse embryos coincides with a metabolic shift from glycolysis to OXPHOS—a phase marked by elevated cytochrome c oxidase activity (Schaetzlein et al. 2004; Hashimoto et al. 2017) and increased ROS levels (Deluao et al. 2022)—suggests that mitochondrial metabolism may also play a positive role in supporting telomerase-driven telomere elongation. We observed that cybrids generated using platelets from Long1 and Long3 donors with long leukocyte telomeres and possible maternal inheritance of long TL had longer telomeres than the recipient Rho^0 cells. This suggests that, similar to early embryogenesis, increased mitochondrial activity during early cybrid formation may be associated with telomere elongation. Our findings further implicate CI in this process, as mitochondria from Long1 and Long3 exhibited high CI activity. Whether and how the centenarian-linked K1a mtDNA of Long3 contributes to telomere elongation in the cybrids is still unclear. As a defective aerobic production of ATP, linked to the ATP6 A177T variant, was proposed to account for the lack of mtDNA K haplogroup in Finnish elite endurance athletes (Niemi et al. 2005), we hypothesize that, by reducing ATP aerobic production, ROS production decreases, thus providing

a possible explanation to this longevity-associated mtDNA (Eynon et al. 2011). Consistent with this, Long3 cybrids showed a distinct response to FCCP uncoupling agent as, unexpectedly, respiration could not be restored in cells with oligomycin-inhibited ATP synthase, suggesting a defective ability in increasing oxygen consumption rate to face an energy demand increase (Fig S6). This could be related to the location of the A177T variant in a crucial region of ATP6, along the proton pore (Ganetzky et al. 2019) (Fig S7). Strikingly, 32.7% of the genetically homogeneous population of Ashkenazi Jews express the ATP6 A177T variant (Ruiz-Pesini et al. 2007). As telomeres from Ashkenazy centenarians blood cells are longer than in control groups (Atzmon et al. 2010), it will be interesting to test the link to the m.G9055>A variant encoding ATP6 A177T.

In summary, our data indicate that low levels of mitochondrial ROS, combined with potent CI activity, may be key for a mtDNA-driven maternal inheritance of long telomeres (Fig 5D). The Japanese m.C5178A longevity-associated variant in the *ND2* gene (Tanaka et al. 1998) further supports an important role for CI in promoting mitochondrial fitness, and possibly TL regulation. Our findings that certain mitochondrial genomes may support telomere elongation are also relevant to three-parent *in vitro* fertilization, a technique that uses donor eggs to prevent the transmission of mitochondrial diseases from mother to child (Callaway et al. 2023). Future work will be necessary to investigate how mitochondrial activity may be involved and whether this is linked to the nucleotide metabolism that recently emerged as an important regulator of telomerase activity (Mannherz et al. 2023; Tummala et al. 2024).

Materials and Methods

Human study participants

Blood samples were obtained from a total of 491 healthy donors. Cohort characteristics are as follows: 261 females and 230 males, median age of 26.3 y (7 days-99.2 y). Protocols were approved by the CHEF institutional Ethics committee and written informed consents were obtained from all 18 year-old or over volunteers. For children below 18, left-over blood samples were obtained through the Cliniques universitaires Saint-Luc after screening for inclusion.

Leukocyte purification

Blood samples were collected in EDTA tubes and kept at room temperature for a maximum of 48 h before processing. Leukocytes were purified after erythrocyte lysis with ice-cold 0.155 M NH_4Cl (Sigma-Aldrich), 0.01 M $KHCO_3$ (Sigma-Aldrich) and 0.1 mM EDTA (Sigma-Aldrich) solution as described (Baerlocher et al. 2006). Leukocytes were then resuspended in hybridization buffer (5 % dextrose/10 mM HEPES/0.1 % BSA), and frozen at -80 °C in 80 % FBS (Cytiva)/20 % DMSO (Sigma-Aldrich).

Flow-FISH

The average telomere length (TL) was measured in peripheral blood leucocytes by flow cytometry combined with FISH (Flow-FISH), using bovine thymocytes as reference as previously described (Baerlocher et al. 2006). Telomere length of bovine thymocytes was measured by telomere restriction fragment (TRF) analysis (see below). TL was evaluated in lymphocyte and granulocyte populations distinguished by LDS751 staining of DNA as described (Baerlocher et al. 2006). The telomeric PNA probe was as follows: FITC-OO-CCCTAACCCTAACCCTAA (Panagene). Values obtained for TL in lymphocytes and granulocytes are provided in Table S1.

Genomic DNA extraction

Genomic DNA was extracted by overnight digestion at 45°C with 100 µg/mL proteinase K (Sigma-Aldrich) in lysis buffer (10 mM Tris–HCl, 10 mM EDTA, 1 % SDS; pH 8.0) followed by DNA purification with 25:24:1 phenol–chloroform–isoamyl alcohol (Sigma-Aldrich) and precipitation in isopropanol (Thermo Fisher Scientific) and 0.3 M sodium acetate; pH 5.5 (Sigma-Aldrich). gDNA was subsequently treated with 0.2 mg/mL RNAse A (Thermo Fisher Scientific) for 1 h at 37 °C, purified, and precipitated again as described above. DNA concentration, purity and integrity were evaluated with Nanodrop (Thermo Fisher Scientific).

MtDNA subhaplogroup identification

PCR reactions were performed on 20-50 ng total DNA using GoTaq® G2 DNA Polymerase (Promega) and the primers provided in Table S2 so as to cover the entire mtDNA sequence (Huebbers et al. 2015). PCR program was as follows: 3 min at 95 °C followed by 40 cycles of 95 °C for 45 s, 47/50/55 °C for 45 s, and 72 °C for 1 min, with a final step at 72 °C for 5 min. PCR products were loaded on 1 % agarose gel (Eurogentec), stained with 0.5 µg/mL ethidium bromide (Sigma-Aldrich) and extracted from the gel using SmartPure Gel Kit (Eurogentec), according to the manufacturer's instructions, followed by Sanger sequencing (Azenta/Genewiz). MtDNA subhaplogroups were identified using MITOMASTER tool on mitomap.org website.

MtDNA content quantification

MtDNA content quantification was performed by qPCR on 60 ng of total DNA, using KAPA SYBR FAST (Sigma-Aldrich) and primer sequences (Huebbers et al. 2015) provided in Table S2.

Cell culture and treatments

143B cells and cybrids were grown in DMEM high glucose (4.5 g/L) supplemented with 10 % FBS (Cytiva) and 1 % Penicillin/Streptomycin (Capricorn Scientific). 143B Rho0 cells were grown in DMEM high glucose supplemented with 0.11 g/L pyruvate (Thermo Fisher Scientific), 10 % FBS (Cytiva), 50 μg/mL uridine (Sigma-Aldrich) and 1 % Penicillin/Streptomycin (Capricorn Scientific). For the subcloning of 143B Rho^0 population, cells were treated exactly as if they would undergo fusion with platelets and kept throughout the cloning process in Rho^0 culture medium. All cell lines were regularly checked for mycoplasma contamination. For this, 100 µL of culture medium were heated at 95°C for 5 min before spinning down. qPCR reactions were performed on 2 µL of the supernatant as described previously (Dreolini et al. 2020) using primers listed in Table S2.

Isolation of human platelets

Blood was collected in 8.5 mL-CPDA tubes (Sarstedt) and centrifuged at 330 x *g* for 20 min at 22 °C. The upper platelet-rich plasma fraction was treated with 4 µg/mL eptifibatide (GlaxoSmithKline) and 1 U/mL apyrase (Sigma-Aldrich) on ice before centrifugation at 800 x *g* for 10 min at room temperature. The pellet was resuspended into 5 mL physiological saline solution containing 4 µg/mL eptifibatide and 1 U/mL apyrase. Platelets were counted and diluted with the saline solution to obtain 10^5 platelets/µL and stored for 30-45 min at 37 °C. 40 x 10^6 platelets were then transferred into a 2 mL Eppendorf tube, centrifuged at 800 x *g* for 10 min at room temperature and directly processed for fusion with 143B Rho^0 cells.

Cybrid formation

Cybrids were obtained as previously described (King et al. 1989). Briefly, 10^6 exponentially growing 143B Rho^0 cells (Prof. G. Attardi, California Institute of Technology, USA) were trypsinized and centrifuged at 290 x *g* for 5 min before resuspension in 2 mL calcium-free DMEM (Thermo Fisher Scientific). Rho^0 cells were slowly added, without mixing, to the freshly-isolated platelet pellet before centrifugation at 200 x *g* for 10 min at RT. Supernatant was discarded and pellet was resuspended in 100 µL PEG 1500 (Sigma-Aldrich) fusion solution (490 µL calcium-free DMEM, 10 µL DMSO, 0.5 g PEG 1500). After homogenization during exactly 1 min, 10 mL DMEM high glucose/pyruvate supplemented with 10 % FBS, 50 µg/mL uridine, 100 µg/mL BrdU (Sigma-Aldrich) and 1 % Penicillin/Streptomycin were added and the cellular suspension was directly distributed into 5 Petri dishes containing 8 mL of the same medium. After 3-5 days, medium was changed and cybrids were selected in DMEM high glucose supplemented with 10 % dialyzed FBS (Thermo Fisher Scientific), 100 µg/mL BrdU and 1 % Penicillin/Streptomycin for 10 days. Colonies from the 5 Petri dishes were isolated with cloning cylinders and transferred into 24-well plates containing DMEM high glucose supplemented with 10 % FBS and 1 % Penicillin/Streptomycin for expansion. Clones were then transferred into flasks and counted for the first time when they had reached 1 to 10 million cells. This time point initiated the calculation of population doublings (PDs), although we estimate that the clones had already gone through at least 19-23 PDs post-fusion. The same procedure was followed for the second fusion of 143B Rho^0 cells with freshly-isolated Aver2 platelets. 5 mM N-Acetyl-L-alanine (NAA, Sigma-Aldrich) or N-Acetyl-L-cysteine (NAC, Sigma-Aldrich) and/or 3 mM Nicotinamide riboside (NR, Sigma-Aldrich) were added directly after the 1 min incubation with PEG. Medium was replaced every 3 days and

drug treatments were maintained until the transfer of the isolated colonies into T25 flasks.

Mitochondrial superoxide assessment by EPR spectroscopy

The electron paramagnetic resonance (EPR) assay is based on the oxidation of Mito-TEMPO-H, a diamagnetic cyclic hydroxylamine that accumulates inside the mitochondria and is transformed into a paramagnetic nitroxide. To isolate the contribution of superoxide to the oxidation of the probe, PEG-SOD2 was used as a control (Scheinok et al. 2020; Dikalov et al. 2011 and 2014; d'Hose et al. 2021). We used a Bruker EMX-Plus spectrometer operating in X-Band (9.85 GHz) and equipped with a PremiumX ultra-low noise bridge and a SHQ high sensitivity resonator. During all the experiments, the EPR cavity was kept at 310 K with a continuous air flow (400 L/h). A mixture was prepared by mixing 37 µL of cell suspension (previously harvested, stock solution $1.5x10^7$/mL of the appropriate medium), 0.5 µL of diethylenetriaminepentaacetic acid (DTPA) (100 mM), 5 µL of PBS (pH 7.4) and 7.5 µL of MitoTempoH (1 mM). The Mito-TEMPO-H (1-hydroxy-4-[2-triphenylphosphosphonio)-acetamido]-2,2,6,6- tetramethylpiperidine) solution (Enzo Life Sciences) was flushed with argon before each experiment to avoid probe oxidation. Control measurements were performed after incubation for 15 min with 200 U/mL PEG-SOD2 (Sigma-Aldrich). The final mixture was transferred in a 12-cm long gas-permeable polytetrafluoroethylene (PTFE) tubing (Zeus) (inside diameter 0.025 in, wall thickness 0.002 in) and folded to be inserted into an open quartz tube. The EPR parameters set in Bruker Xenon Spin fit program were: microwave power, 20 mW; modulation frequency, 100 kHz; modulation amplitude, 0.1 mT; center field, 336.5 mT; sweep width, 1.5 mT; sweep time, 30.48 s. The first EPR acquisition was performed 3 min after the probe was added to the cell mixture. For each biological replicate,

measurements were done in triplicates. Measurements were performed on cybrids (clone #1 for all) between PD43 and PD63. Data were analyzed by performing a double integration on selected regions of peaks and retrieving background values obtained with PEG-SOD2. Full details of the procedure are published elsewhere (d'Hose et al. 2022).

Seahorse analyses

Oxygen consumption rates (OCR) were measured by using the Seahorse XFe96 plate reader (Agilent). All assays were carried out using a seeding density of 10,000 cells/well in non-buffered DMEM, adjusted at pH 7.4. Mitochondrial function parameters (*i.e.* basal and maximal respirations and ATP production-linked OCR) were evaluated, with the XF Cell MitoStress Test (Agilent), after sequential treatment with 1 µM oligomycin, 1 µM FCCP and 0.5 µM rotenone/antimycin A, as previously described (Vander Linden et al. 2021). ETC complex activity was assessed as previously reported[11], with slight modifications. Briefly, 10^4 cells per well were first permeabilized with 1 nM Seahorse XF Plasma Membrane Permeabilizer (Agilent) and respiration was stimulated by adding 10 mM pyruvate, 5 mM malate, and 2 mM ADP. After the baseline scan, 100 nM rotenone was then added to inhibit complex I and 10 mM succinate was injected to establish complex II respiration. Last, 4 µM antimycin A was added to inhibit complex III and 100 µM N,N,N',N'-Tetramethyl-p-phenylenediamine dihydrochloride (TMPD) + 10 mM ascorbate was injected as a complex IV substrate. OCR data were then normalized according to protein content in each experimental well.

Telomere restriction fragment (TRF) length analysis

TRF analyses were performed as described previously (Episkopou et al. 2019) on 2-5 µg of RNAse-treated genomic DNA digested with 20 U *Hinf*I and 20 U *Rsa*I and

using [γ-^{32}P] ATP-labelled $(TAACCC)_4$ probe. Smart Ladder (Eurogentec) was run together with the samples, stained with ethidium bromide and imaged with a ruler. TRF were quantified using the online available WALTER (Web-based Analyser of the Length of Telomeres) software (https://www.ceitec.eu/chromatin-molecular-complexes/rg51/tab?tabId=125#WALTER).

TeSLA analysis

The procedure described previously (Lai et al. 2017) was followed for TeSLA analysis. Primer sequences are provided in Table S2.

Immunofluorescence and fluorescence *in situ* hybridization

Immunofluorescence and FISH experiments were performed as described previously (Episkopou et al. 2019) using the following antibodies and telomeric probe: rabbit anti-53BP1 (Novus Biologicals), Alexa 488 goat anti-rabbit (Invitrogen), mouse anti-Poly(ADP-ribose) (Millipore), Alexa 488 Goat anti-mouse (Abcam), 5'(TYE 563)GGGTtAGGGttAGgGTTAGGGttAGGGttAGGGtTA(TYE 563) (small letters indicate LNA^{TM} modified bases) (Qiagen). For the detection of parylated proteins, cells were grown in the presence of 1 μM PDD00017273 PARG inhibitor (Sigma-Aldrich). For telomeric FISH on metaphase spreads, cells were treated as described previously (Viceconte et al. 2017) and telomeres were probed with 5'(TYE 563)GGGTtAGGGttAGgGTTAGGGttAGGGttAGGGtTA(TYE 563). Images were acquired with the Cell Observer Spinning Disk confocal microscope (Zeiss) with 100× objective and analyzed using ImageJ software (National Institute of Health), while maintaining the same threshold for samples from the same experiment.

Liquid chromatography-mass spectrometry analysis of metabolites

6-well plates with cultured cells were rapidly washed twice with ice cold water and submerged in liquid nitrogen. 300 µL of a solution of 90 % methanol and 10 % chloroform were added, lysates were scraped and transferred to microcentrifuge tubes for centrifugation for 15 min at 4 °C and 22, 000 x *g*. The supernatants were dried in a Speed-Vac vacuum concentrating system and resuspended into 50 µL of 50:50 water:methanol solution. Analyses by LC-MS were performed as previously described (Heremans et al. 2022) based on a method by Coulier et al. (2006). Briefly, 5 µL of sample were analyzed with an Inertsil 3 µm ODS-4 column (150 x 2.1 mm; GL Biosciences) at a flow rate of 0.2 mL/min using an Agilent 1290 HPLC system coupled to an Agilent 6550 Q-TOF MS in negative mode. Mobile phase A consisted of 5 mM hexylamine adjusted to pH 6.3 with acetic acid and phase B of 90 % methanol/10 % 10 mM ammonium acetate adjusted to pH 8.5 with ammonia. The mobile phase profile was set up as follows: 0 – 2 min at 0 % B; 2 – 6 min from 0 to 20 % B; 6 – 17 min from 20 to 31 %B; 17 – 36 min from 31 to 60 % B; 36 – 41 min from 60 to 100 % B; 41 – 51 min at 100 % B; 51 – 53 min from 100 to 0 % B; 53 – 60 min at 0 % B. Compound identification was based on exact mass (<5 ppm) and retention time compared to standards. The areas under the curve of extracted-ion chromatograms of the $[M-H]^-$ forms were determined using MassHunter software (Agilent) and normalized to the mean value of a batch of 150 other metabolites ('total ion current').

Dosage of extracellular glucose and lactate

Glucose and lactate concentrations were measured in extracellular media by using specific enzymatic assays and an ISCUSflex microdialysis analyzer (M Dialysis), as previously described (Vander Linden et al. 2021).

RNA isolation and reverse transcription quantitative real-time PCR

RNA was extracted using TriPure Isolation Reagent (Sigma-Aldrich) according to the manufacturer's instructions. For cDNA synthesis, 1 µg of RNA was retro-transcribed with 200 U MMLV-RT (Thermo Fisher Scientific), 0.2 µg random hexamers (Thermo Fisher Scientific), 20 U RiboLock RNase inhibitor (Thermo Fisher Scientific) and 2 mM dNTP mix. qPCR reactions were performed using KAPA SYBR FAST (Sigma-Aldrich) and the following program: 95°C for 10 min followed by 40 cycles of 95 °C for 15 sec and 60 °C for 30 sec. Primer sequences are provided in Table S2.

Statistics

Statistical analyses were performed using PRISM 8 software. Normality of the data was always checked before statistical tests. Details are provided in the Figure legends. Nomograms for Flow-FISH-based measurements of TL in the healthy population were drawn using the Age-related reference interval function of MedCalc Software (Belgium) based on methods described previously (Wright et al. 1997; Altman 1993; Altman et al. 1993).

Author contributions

M.M., J.-P.D. and A.D. generated the Flow-FISH curves. G.L., I.S., B.B. and A.D. recruited volunteers and helped collecting blood. M.M., B.M. and B.G. contributed to ROS measurement. M.M., E.R. and C.C. contributed to OCR and ETC complex activity measurement and to glycolytic flux evaluation. I.H. and G.B. contributed to metabolite analyses. M.M. and T.A. contributed to transmitochondrial cybrid formation. G.L.B. contributed to PAR-FISH analysis. M.M. performed TRF, TeSLA, RT-qPCR, IF/FISH and qPCR analyses. A.D. and C.C. designed and supervised the study. A.D. wrote the paper.

Acknowledgments

We are grateful to all volunteers for providing blood samples. We thank Sandrine Horman, Marie Octave and Valentine Robaux for help with platelet purification and Géraldine Aubert and Mary Armanios for guidance in Flow-FISH. We are grateful to Victoria Van Regemorter and Caroline Huart for sharing unpublished data on TL in their cohort. We thank Chloé Despontin and Antoine Fattaccioli for technical support, Céline Coquette for help with blood collection and Mélina Vaurs, Nausica Arnoult and Patrick Revy for critical reading of the manuscript. We thank Boutaina Boulouadnine for help with Alphafold. We are grateful to the de Duve Institute and the Fonds National de la Recherche Scientifique (FNRS) for their continued support.

Conflicts of interest

The authors declare no conflicts of interest.

References

Alder, J. K., J.J. Chen, L. Lancaster, et al. 2008. Short telomeres are a risk factor for idiopathic pulmonary fibrosis. *Proc Natl Acad Sci U S A* **105**, 13051-13056, doi:10.1073/pnas.0804280105.

Altman, D.G. 1993. Construction of age-related reference centiles using absolute residuals. *Stat Med* **12**, 917-924, doi:10.1002/sim.4780121003.

Altman, D.G., and L.S. Chitty. 1993. Design and analysis of studies to derive charts of fetal size. *Ultrasound Obstet Gynecol* **3**, 378-384, doi:10.1046/j.1469-0705.1993.03060378.x.

Asghar, M., S. Bensch, M. Tarka, B. Hansson, and D. Hasselquist. 2015. Maternal and genetic factors determine early life telomere length. *Proc Biol Sci* **282**, 20142263, doi:10.1098/rspb.2014.2263.

Atzmon, G. *et al.* 2010. Genetic variation in human telomerase is associated with telomere length in Ashkenazi centenarians. *Proc Natl Acad Sci U S A* **107 Suppl 1**, 1710-1717, doi: 10.1073/pnas.0906191106

Aubert, G., G. M. Baerlocher, I. Vulto, S. S. Poon, and P.M. Lansdorp. 2012. “Collapse of telomere homeostasis in hematopoietic cells caused by heterozygous mutations in telomerase genes." *PLoS Genet* **8**, e1002696, doi:10.1371/journal.pgen.1002696.

Baerlocher, G. M., I. Vulto, G. de Jong, and P.M. Lansdorp. 2006. “Flow cytometry and FISH to measure the average length of telomeres (flow FISH).” *Nat Protoc* **1**, 2365-2376, doi:10.1038/nprot.2006.263.

Barnes, R. P., E. Fouquerel, and P.L. Opresko. 2019. The impact of oxidative DNA damage and stress on telomere homeostasis. *Mech Ageing Dev* **177**, 37-45, doi:10.1016/j.mad.2018.03.013.

Barnes, R.P., M. de Rosa, S.A. Thosar, et al. 2022. Telomeric 8-oxo-guanine drives rapid premature senescence in the absence of telomere shortening. *Nat Struct Mol Biol* **29**, 639-652, doi: 10.1038/s41594-022-00790-y.

Belenky, P., K. L. Bogan, and C. Brenner. 2007. NAD+ metabolism in health and disease. *Trends Biochem Sci* **32**, 12-19, doi:10.1016/j.tibs.2006.11.006.

Bertoldo, M. J., D.R. Listijono, W.J. Ho, et al. 2020. NAD(+) Repletion Rescues Female Fertility during Reproductive Aging. *Cell Rep* **30**, 1670-1681 e1677, doi:10.1016/j.celrep.2020.01.058.

Broer, L., V. Codd, D.R. Nyholt, et al. 2013. Meta-analysis of telomere length in 19,713 subjects reveals high heritability, stronger maternal inheritance and a paternal age effect. *Eur J Hum Genet* **21**, 1163-1168, doi:10.1038/ejhg.2012.303.

Callaway, E. 2023. First UK children born using three-person IVF: what scientists want to know. *Nature* **617**, 443-444, doi:10.1038/d41586-023-01585-x

Campisi, J., J. K. Andersen, P. Kapahi, and S. Melov. 2011. Cellular senescence: a link between cancer and age-related degenerative disease? *Semin Cancer Biol* **21**, 354-359, doi:10.1016/j.semcancer.2011.09.001.

Castaneda, V., A. Haro-Vinueza, I. Salinas, A. Caicedo, and M.A. Mendez. 2022. The MitoAging Project: Single nucleotide polymorphisms (SNPs) in mitochondrial genes and their association to longevity. *Mitochondrion* **66**, 13-26, doi:10.1016/j.mito.2022.06.008.

Coulier, L., R. Bas, S. Jespersen et al. 2006. Simultaneous quantitative analysis of metabolites using ion-pair liquid chromatography-electrospray ionization mass spectrometry. *Anal Chem* **78**, 6573-6582, doi:10.1021/ac0607616.

d'Adda di Fagagna, F., M.P. Hande, W.M. Tong, et al. 1999. Functions of poly(ADP-ribose) polymerase in controlling telomere length and chromosomal stability. *Nat Genet* **23**, 76-80, doi:10.1038/12680.

d'Hose, D., P. Danhier, H. Northshield, et al. 2021. A versatile EPR toolbox for the simultaneous measurement of oxygen consumption and superoxide production. *Redox Biol* **40**, 101852, doi:10.1016/j.redox.2020.101852.

d'Hose, D., and B. Gallez. 2022. Measurement of Mitochondrial (Dys)Function in Cellular Systems Using Electron Paramagnetic Resonance (EPR): Oxygen Consumption Rate and Superoxide Production. *Methods Mol Biol* **2497**, 83-95, doi:10.1007/978-1-0716-2309-1_5.

de Lange, T. 2018. Shelterin-Mediated Telomere Protection. *Annu Rev Genet* **52**, 223-247, doi:10.1146/annurev-genet-032918-021921.

Deluao, J.C., Y. Winstanley, R.L. Robker, et al. 2022. OXIDATIVE STRESS AND REPRODUCTIVE FUNCTION: Reactive oxygen species in the mammalian pre-implantation embryo. *Reproduction* **164**, F95-F108, doi:10.1530/REP-22-0121.

Demanelis, K., F. Jasmine, L.S. Chen, et al. 2020. Determinants of telomere length across human tissues. *Science* **369**, doi:10.1126/science.aaz6876.

Dreolini, L., M. Cullen, E. Yung et al. 2020. A Rapid and Sensitive Nucleic Acid Amplification Technique for Mycoplasma Screening of Cell Therapy Products. *Mol Ther Methods Clin Dev* **17**, 393-399, doi:10.1016/j.omtm.2020.01.009.

Dikalov, S.I., I.A. Kirilyuk, M. Voinov, and I.A. Grigor'ev. 2011. EPR detection of cellular and mitochondrial superoxide using cyclic hydroxylamines. *Free Radic Res* **45**, 417-430, doi:10.3109/10715762.2010.540242.

Dikalov, S.I., and D.G. Harrison. 2014. Methods for detection of mitochondrial and cellular reactive oxygen species. *Antioxid Redox Signal* **20**, 372-382, doi:10.1089/ars.2012.4886.

Entringer, S., E.S. Epel, R. Kumsta, et al. 2011.Stress exposure in intrauterine life is associated with shorter telomere length in young adulthood. *Proc Natl Acad Sci USA* **108**, E513-518, doi: 10.1073/pnas.1107759108.

Episkopou, H., A. Diman, E. Claude, N. Viceconte, and A. Decottignies. 2019. TSPYL5 Depletion Induces Specific Death of ALT Cells through USP7-Dependent Proteasomal Degradation of POT1. *Mol Cell* **75**, 469-482 e466, doi:10.1016/j.molcel.2019.05.027.

Eynon, N., M. Moran, R. Birk, and A. Lucia. 2011. The champions' mitochondria: is it genetically determined? A review on mitochondrial DNA and elite athletic performance. *Physiol Genomics* **43**, 789-798, doi:10.1152/physiolgenomics.00029.2011.

Fouquerel, E., R.P. Barnes, S. Uttam, et al. 2019. Targeted and Persistent 8-Oxoguanine Base Damage at Telomeres Promotes Telomere Loss and Crisis. *Mol Cell* **75**, 117-130 e116, doi:10.1016/j.molcel.2019.04.024.

Froidure, A., M. Mahieu, D. Hoton, et al. 2020. Short telomeres increase the risk of severe COVID-19. *Aging (Albany NY)* **12**, 19911-19922, doi:10.18632/aging.104097.

Ganetzky, R. D., C. Stendel, E.M. McCormick, et al. 2019. MT-ATP6 mitochondrial disease variants: Phenotypic and biochemical features analysis in 218 published cases and cohort of 14 new cases. *Hum Mutat* **40**, 499-515, doi:10.1002/humu.23723.

Hashimoto, S., N. Morimoto, M. Yamanaka, et al. 2017. Quantitative and qualitative changes of mitochondria in human preimplantation embryos. *J Assist Reprod Genet* **34**, 573-580, doi: 10.1007/s10815-017-0886-6.

Heremans, I.P., F. Caligiore, I. Gerin et al. 2022. Parkinson's disease protein PARK7 prevents metabolite and protein damage caused by a glycolytic metabolite. *Proc Natl Acad Sci U S A* **119**, doi:10.1073/pnas.2111338119.

Huebbers, C.U., A.C. Adam, S.F. Preuss et al. 2015. High glucose uptake unexpectedly is accompanied by high levels of the mitochondrial ss-F1-ATPase subunit in head and neck squamous cell carcinoma. *Oncotarget* **6**, 36172-36184, doi:10.18632/oncotarget.5459.

Ivanova, R., V. Lepage, D. Charron, and F. Schachter. 1998. Mitochondrial genotype associated with French Caucasian centenarians. *Gerontology* **44**, 349, doi:10.1159/000022041.

King, M. P., and G. Attardi. 1989. Human cells lacking mtDNA: repopulation with exogenous mitochondria by complementation. *Science* **246**, 500-503, doi:10.1126/science.2814477.

Lai, T.P., N. Zhang, J. Noh et al. 2017. A method for measuring the distribution of the shortest telomeres in cells and tissues. *Nat Commun* **8**, 1356, doi:10.1038/s41467-017-01291-z.

López-Otín, C., M.A. Blasco, L. Partridge, M. Serrano, and G. Kroemer. 2023. Hallmarks of aging: an expanding universe. *Cell* **186**, 243-278, doi: 10.1016/j.cell.2022.11.001.

Mannherz, W., and S. Agarwal. 2023. Thymidine nucleotide metabolism controls human telomere length. *Nat Genet* **55**, 568-580, doi:10.1038/s41588-023-01339-5.

Mundstock, E., E.E. Sarria, H. Zatti, et al. 2015. Effect of obesity on telomere length: Systematic review and meta-analysis. *Obesity (Silver Spring)* **23**, 2165-2174, doi:10.1002/oby.21183.

Nersisyan, L., M. Nikoghosyan, Genome of the Netherlands consortium, and A. Arakelyan. 2019. WGS-based telomere length analysis in Dutch family trios implicates stronger maternal inheritance and a role for RRM1 gene. *Sci Rep* **9**, 18758, doi:10.1038/s41598-019-55109-7.

Niemi, A. K., and K. Majamaa. 2005. Mitochondrial DNA and ACTN3 genotypes in Finnish elite endurance and sprint athletes. *Eur J Hum Genet* **13**, 965-969, doi:10.1038/sj.ejhg.5201438.

Oexle, K., and A. Zwirner. 1997. Advanced telomere shortening in respiratory chain disorders. *Hum Mol Genet* **6**, 905-908, doi:10.1093/hmg/6.6.905.

Passos, J. F., G. Saretzki, and T. von Zglinicki. 2007. DNA damage in telomeres and mitochondria during cellular senescence: is there a connection? *Nucleic Acids Res* **35**, 7505-7513, doi:10.1093/nar/gkm893.

Qian, W., N. Kumar, V. Roginskaya, et al. 2019. Chemoptogenetic damage to mitochondria causes rapid telomere dysfunction. *Proc Natl Acad Sci U S A* **116**, 18435-18444, doi:10.1073/pnas.1910574116.

Ross, O.A., R. McCormack, M.D. Curran, et al. 2001. Mitochondrial DNA polymorphism: its role in longevity of the Irish population. *Exp Gerontol* **36**, 1161-1178, doi:10.1016/s0531-5565(01)00094-8.

Ruiz-Pesini, E., M.T. Lott, V. Procaccio, et al. 2007. An enhanced MITOMAP with a global mtDNA mutational phylogeny. *Nucleic Acids Res* **35**, D823-828, doi:10.1093/nar/gkl927.

Rzasa, R., M. Glassman, W.E. Bentley, S. Chen, D.L. Kelly, and G.F. Payne. 2021. Association of acute psychological stress with oxidative stress: evidence from serum analysis. *Redox Biol* **47**, 102138, doi: 10.1016/j.redox.2021.102138.

Salim, S. 2014. Oxidative stress and psychological disorders. Curr Neurophrmacol 12, 140-147, doi: 10.2174/1570159X11666131120230309.

Schaetzlein, S., A. Lucas-Hahn, E. Lemme, et al. 2004. Telomere length is reset during early mammalian embryogenesis. *Proc Natl Acad Sci U S A* **101**, 8034-8038, doi: 10.1073/pnas.0402400101.

Scheinok, S., T. Capeloa, P.E. Porporato, P. Sonveaux, and B. Gallez. 2020. An EPR Study Using Cyclic Hydroxylamines To Assess The Level of Mitochondrial ROS in Superinvasive Cancer Cells. *Cell Biochem Biophys* **78**, 249-254, doi:10.1007/s12013-020-00921-6.

Schneider, C.V., K.M. Schneider, A. Teumer, et al. 2022. Association of telomere length with risk of disease and mortality. *JAMA Intern Med* **182**, 291-300, doi: 10.1001/jamainternmed.2021.7804.

Stock, A.J., S. Ayyar, A. Kashyap, et al. 2023. Boosting NAD ameliorates hematopoietic impairment linked to short telomeres in vivo. *Geroscience* **45**, 2213-2228, doi:10.1007/s11357-023-00752-2.

Sun, C., K. Wang, A.J. Stock, et al. 2020. Re-equilibration of imbalanced NAD metabolism ameliorates the impact of telomere dysfunction. *EMBO J* **39**, e103420, doi:10.15252/embj.2019103420.

Tanaka, M., J.S. Gong, J. Zhang, M. Yoneda, and K. Yagi. 1998. Mitochondrial genotype associated with longevity. *Lancet* **351**, 185-186, doi:10.1016/S0140-6736(05)78211-8 .

Tummala, H., A. Walne, R. Buccafusca, et al. 2024. Germline thymidylate synthase deficiency impacts nucleotide metabolism and causes dyskeratosis congenita. *Am J Hum Genet* **109**, 1472-1483, doi:10.1016/j.ajhg.2022.06.014.

Vander Linden, C., C. Corbet, E. Bastien et al. 2021. Therapy-induced DNA methylation inactivates MCT1 and renders tumor cells vulnerable to MCT4 inhibition. *Cell Rep* **35**, 109202, doi:10.1016/j.celrep.2021.109202.

Viceconte, N., M.-S. Dheur, E. Majerova et al. 2017. Highly Aggressive Metastatic Melanoma Cells Unable to Maintain Telomere Length. *Cell Rep* **19**, 2529-2543, doi:10.1016/j.celrep.2017.05.046.

Winstanley, Y.E., R.D. Rose, A.P. Sobinoff, et al. 2025. Telomere length in offspring is determined by mitochondrial-nuclear communication at fertilization. *Nat Commun* **16**, 2527, doi: 10.1038/s41467-025-57794-7.

Wright, E.M., and P. Royston. 1997. Simplified estimation of age-specific reference intervals for skewed data. *Stat Med* **16**, 2785-2803, doi:10.1002/(sici)1097-0258(19971230)16:24<2785::aid-sim797>3.0.co;2-z.

Zhuo, Y., H. Luo, and K. Zhang. 2012. Leber hereditary optic neuropathy and oxidative stress. *Proc Natl Acad Sci U S A* **109**, 19882-19883, doi:10.1073/pnas.1218953109.

Figure legends

Figure 1. Establishment of Flow-FISH reference curves for TL. A. The age-related reference interval and centiles were calculated after telomere length measurement by Flow-FISH in lymphocytes obtained from 491 healthy donors. The P50 curve is shown in dark blue. Other percentile curves are shown as indicated in the legend. **B.** Same as A in granulocytes. **C.** Comparison of Flow-FISH curves obtained in lymphocytes from healthy donors by Alder et al. (black squares), Aubert et al. (red circles) and us (blue triangles).

Figure 2. K1a and H1b1e mitochondrial suhaplogroups are linked to long telomeres. A. Snapshot of TL in lymphocytes and granulocytes of the seven selected donors. **B.** Overview of the variants showing both a change in the amino acid sequence and an overall frequency of less than 10% in Mitomap database in the mtDNA coding regions of the donors. The variant frequency in the subhaplogroup of each donor is indicated in the last column. **C.** TL of Long1 (H1b1e), Long2 (T2b4a), Long3 (K1a4a1) and their relatives is shown as indicated in the legend. Orange triangles show TL in unrelated K1a11b and K1a4a1a2b donors. **D.** Frequency of donors with the ATP6 A177T variant among n selected donors with lymphocyte TL in the indicated ranges (<P50, between P50 and <P90 and ≥P90).

Figure 3. Mitochondrial superoxide production in cybrids inversely correlates with TL in lymphocytes. A. Mitochondrial superoxide production measured by electron paramagnetic resonance and corrected for background using PEG-SOD2 in clone #1 from Long1, 2 and 3 (Long), Aver1 and 2 (Aver) and Short1 and 2 (Short) cybrids. n measurements from 2 biological replicates with 3 technical replicates. Mean

± SEM. Kruskal-Wallis test. **B.** Correlation between lymphocyte TL (in kb, adjusted to 50 yo) and average mitochondrial superoxide production measured in cybrids from the corresponding donors. **C.** Complex IV activity in 143B and in the cybrids. Values were normalized to the activity of complex II, which is entirely nuclear-encoded. n measurements per cell line from 2 biological replicates. One-way ANOVA. ns: p>0.05. **D.** The F63 residue of COX1, mutated into a leucine residue in Short1 donor, is highlighted in pink. The nearby H61 residue, located in direct proximity of the heme A group, is shown (genecards.org).

Figure 4. Mitochondrial genomes modulate telomere length and integrity of Rho^0 recipient cells. A. Left: Representative Southern blot analysis (TRF) of telomeres in 143B Rho^0 recipient cells and in two independent cybrid clones from each donor at the first PDs post-selection. Right: Quantification of TRF on four independent cybrid clones for each. Mean ± SEM. One-way ANOVA. ns: p>0.05. **B.** Left: TeSLA analysis of TL in clone #1 of the indicated cybrids at similar PD values and in 143B Rho^0 recipient cells. n=1. Right: Frequency of telomeres with length <1kb in 143B Rho^0 cells, Long1, Long3 and Long2 cybrids calculated on n telomeres. **C.** Left: Representative pictures of telomere dysfunction-induced foci (TIF) detection by co-localization of telomeres (red FISH probe) with 53BP1 DNA damage marker (green). White arrowheads indicate TIF. Blue: DAPI. Scale bar: 5 μm. Right: TIF quantification in clone #1 of all cybrids (first PDs post-selection) and in 143B Rho^0 cells. n=47-63 nuclei. Mean ± SEM. Kruskal-Wallis test. ns: p>0.05. **D.** Visualisation of telomere fusions (white arrowheads) in Long2 cybrid cells at PD7. 143B Rho^0 and Long3 cybrids are shown as controls. Telomeres are detected by FISH (red) and DAPI stains DNA (blue). Scale bar: 5 μm. **E.** Complex I activity in 143B and in the cybrids. Values were normalized to the activity

of complex II which is entirely nuclear-encoded. n measurements from 2 biological replicates on clone #1 from all: at PD 4-7 or PD 16-24 post-selection. Mean ± SEM. Kruskal-Wallis test. ns: p>0.05. **F.** Correlation between TL in the cybrids at early PDs and average ratios of complex I/II activity. Color code as in E. **G.** Expression of *NAMPT* and *NAPRT1* genes from the NAD^+ salvage pathway in cybrid clones #1, #2 and #3 (PD≥5 post-selection) from donors with either normal (Long1, Long3, Aver1, Short1 or Short2) or low (Long2, Aver2) complex I activity. Values were normalized to *ACTB* and to the ratios measured in 143B cells. Color code as in E. n=3 biological replicates. Mean ± SEM. Two-tailed Student's *t* tests.

Figure 5. Telomere shortening in cybrids from donor with low complex I activity is counteracted by antioxidant and NAD^+ precursor. A. Representative TRF analysis of TL in cybrids obtained by fusion between Aver2 platelets and 143B Rho^0 recipient cells in the presence of the indicated treatments or in the absence of added drug (-). 5 mM N-acetyl-L-cysteine (NAC), 5 mM N-acetyl-L-alanine (NAA, control) and/or 3 mM nicotinamide riboside (NR) were added at the time of the fusion and kept until clone isolation. **B.** TL was measured in the following numbers of independent clones: 5 (NAA), 7 (NAC), 8 (NAC + NR or NAA + NR) and the percentage of clones with average TL>2.5 kb was calculated. **C.** Representative images and quantification of telomeric parylation in Aver2 cybrids shown in panel A, comparing cells that did or did not exhibit telomere shortening during the initial PDs following cybridisation. Parylation was detected by IF (green) in the presence or PARG inhibitor; telomeres were detected by FISH (red) and DNA was stained with DAPI (blue). Scale bar: 5 μm. n=94-116 nuclei were counted for each clone. Mean ± SEM. Two-tailed Mann-Whitney test. **D.** Model. In transmitochondrial cybrids, the reintroduction of mitochondria into Rho^0 cells induces a metabolic shift from glycolysis to OXPHOS. When platelets from

donors with long leukocyte telomeres and mitochondria exhibiting low ROS production and high CI activity are used, TL increases in the recipient cells. In contrast, mitochondria with low CI activity lead to a marked telomere shortening in cybrids.

Supplementary figure legends

Figure S1. Body mass index (BMI) was calculated in donors classified according to the percentile of TL in their lymphocytes as indicated. Min, Lower quartile, Median, Upper quartile, Max. None of the comparisons gave significant difference using the Kruskal-Wallis test. ns: $p>0.05$.

Figure S2. Telomere length, measured by Flow-FISH, in the lymphocytes of donors with either m.G9055 (ATP6 A177, red squares) or m.G9055>A (ATP6 A177T, black squares). The P50 curve is shown in dark blue.

Figure S3. Quantification of mtDNA content by qPCR in four independent cybrid clones from the seven donors at early PDs, normalized to h*TR* genomic DNA content and to 143B.

Figure S4. A. Mitochondrial superoxide production measured by EPR and corrected for background using PEG-SOD2 in cybrid clones #1 from the seven donors. n measurements from 2 biological replicates and technical replicates. Mean ± SEM. Kruskal-Wallis test. **B.** Lactate and glucose concentrations measured by enzymatic colorimetric assay in clones #1 of the cybrids. Lactate/glucose ratios were normalized to 143B. n=3 biological replicates. Mean ± SEM. **C.** ATP and ADP levels measured by

LC/MS in clones #1 of cybrids. n=3 biological replicates. ATP/ADP ratios were normalized to 143B. Mean ± SEM.

Figure S5. A. Left: TRF analysis of TL in independent clones from Long1 and Long3 cybrids at first PDs and in subclones of the 143B Rho^0 cell line. Right: Quantification of TL in a total of seven Long1 or Long3 cybrid clones and seven 143B Rho^0 subclones. Mean ± SEM. One-way ANOVA. **B.** Evolution of TL over PDs, measured by TRF, in clones #1 of Long1 and Long3 cybrids. n=1-3 replicates/PD. Mean ± SEM when indicated. **C.** TRF analysis of TL in clone #1 of Aver2 cybrid over successive PDs as indicated. **D.** Quantifications of TL over PDs for clones #1 of Long2 and Aver 2 cybrids from TRF analyses. **E.** Evolution of proliferation rate of clones #1 from cybrids over time. Proliferation rate was calculated as the number of PD/day between the passages indicated on the X axis (P2: passage #2, ..). Long2 and Aver2 cybrids show a progressive recovery of their proliferation rate that correlates with the recovery of TL detected in D.

Figure S6. **A**. Overview of the Seahorse Cell Mito Stress Test used to evaluate basal and maximal oxygen consumption rates (OCR), the ATP-linked OCR and the proton leak contribution to OCR. **B.** OCR values in 2-4 different cybrid clones from each donor in the conditions described in A. n=2-5 biological replicates with technical replicates. Mean ± SEM.

Figure S7. Comparison of the tri-dimensional structure of ATP6 A177T with the reference protein using Alphafold. The reference protein is shown in dark blue and the variant in light blue. The A177 residue appears in red and the T177 variant residue in yellow.

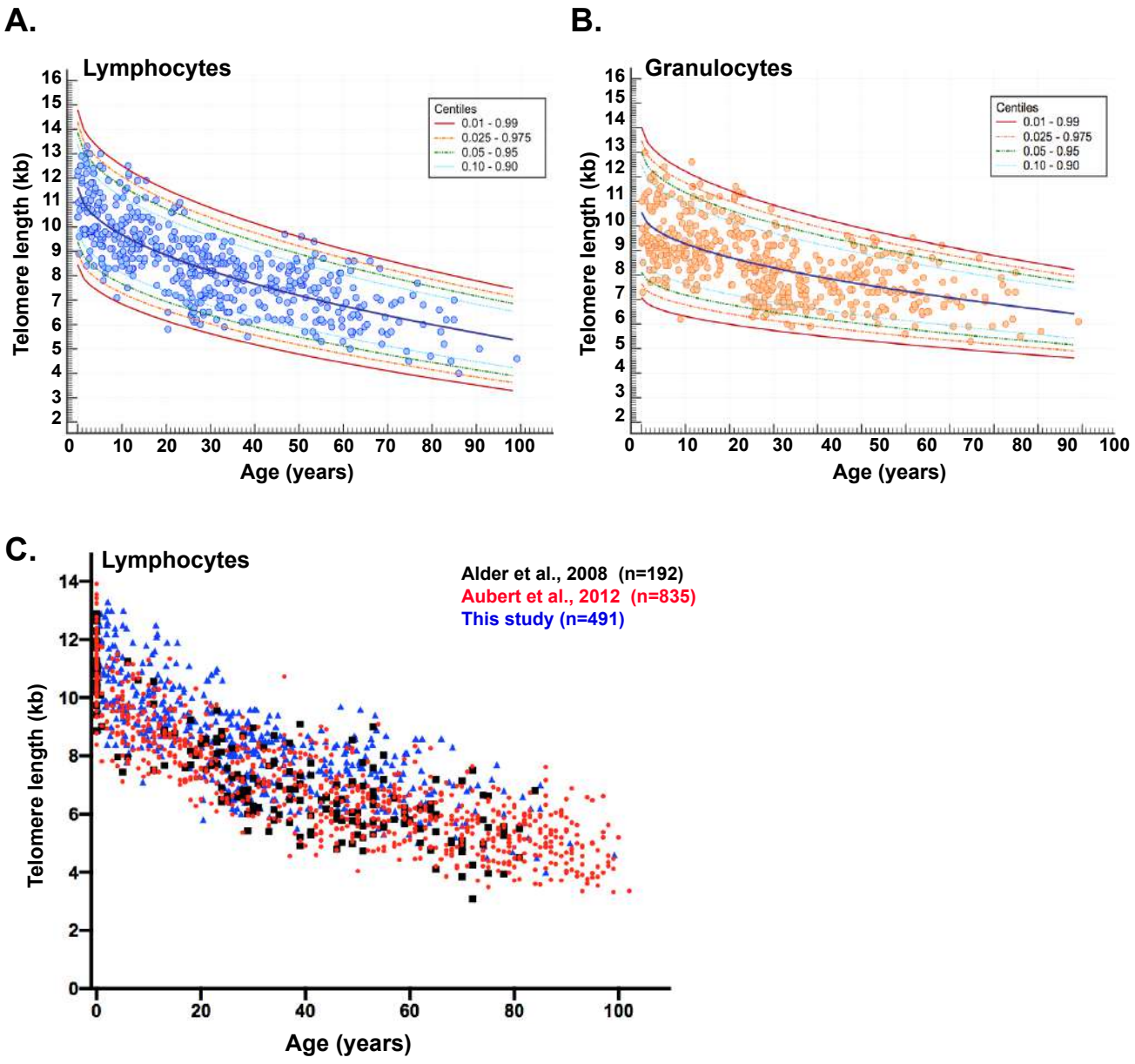

Figure 1

A.

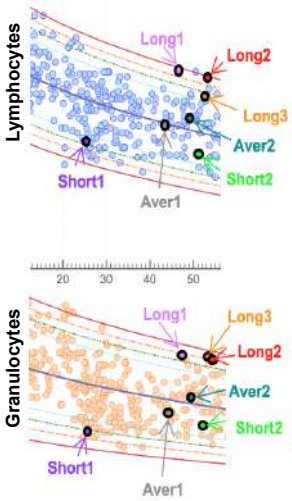

B.

	Subhaplogroup	Rare variant (Complex)	Variant frequency Overall	Variant frequency In subhaplogroup
Long1	H1b1e	ND1 T164A (CI)	0.8%	29.5%
Long2	T2b4a	ND2 N150D (CI)	5.8%	100%
Long3	K1a4a1	ATP6 A177T (CV)	5.4%	99%
		COB F18L (CIII)	8.8%	99.6%
Aver1	H6a1a	ND4 S418P (CI)	0.06%	0%
		ND4 I165T (CI)	0.7%	51.8%
Aver2	H56b			
Short1	H	COX1 F63L (CIV)	0.002%	0%
		ATP8 M16L (CV)	0.004%	0.2%
Short2	H2a2a1			

C.

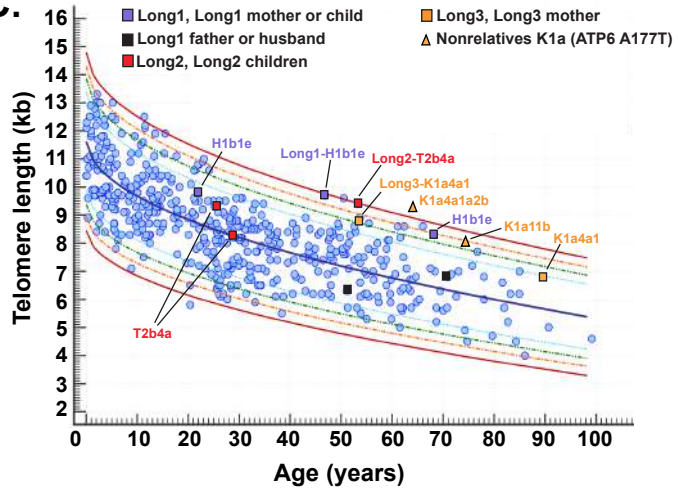

D.

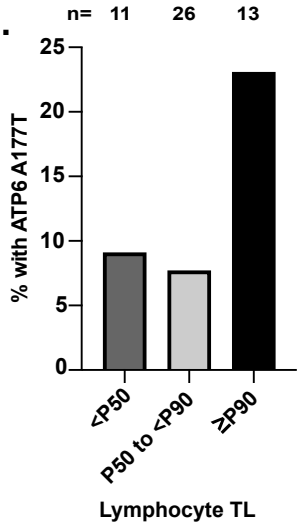

Figure 2

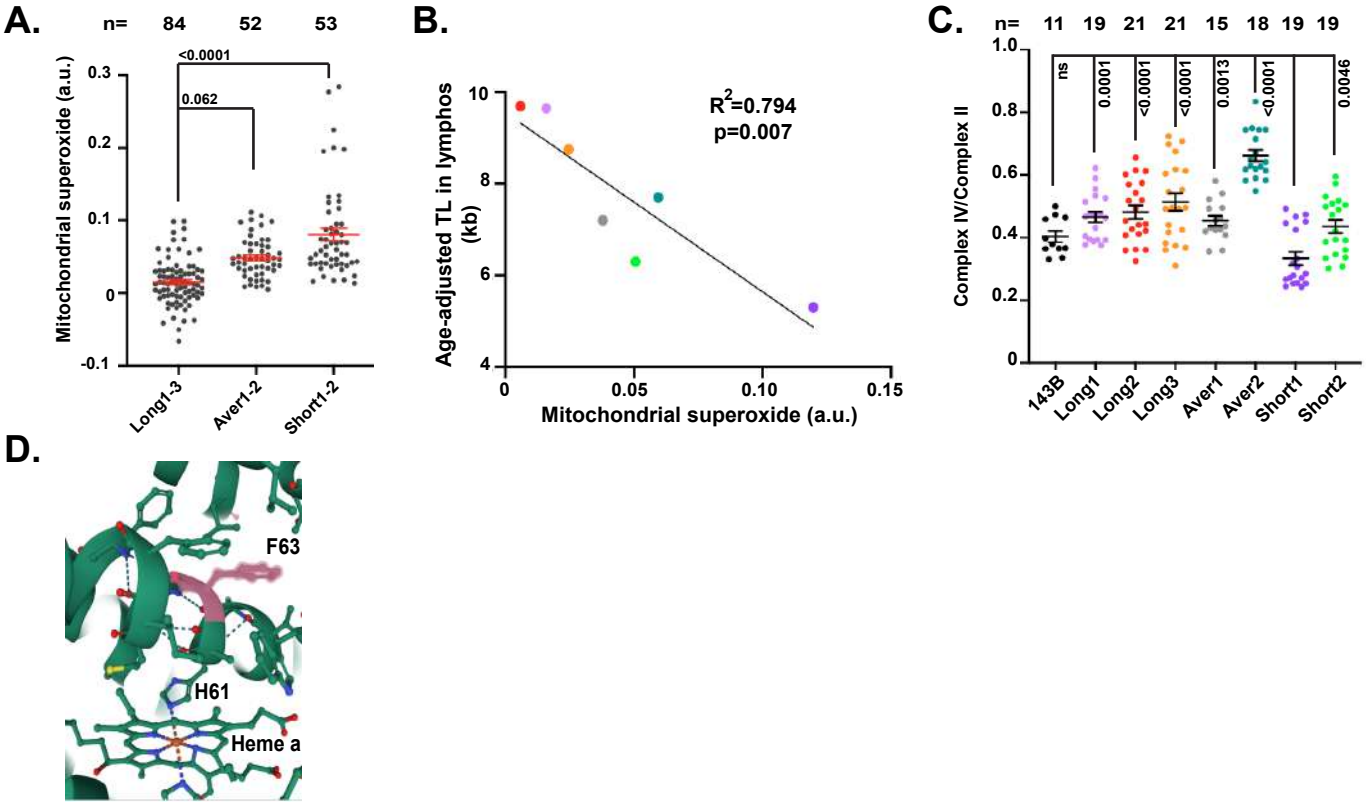

Figure 3

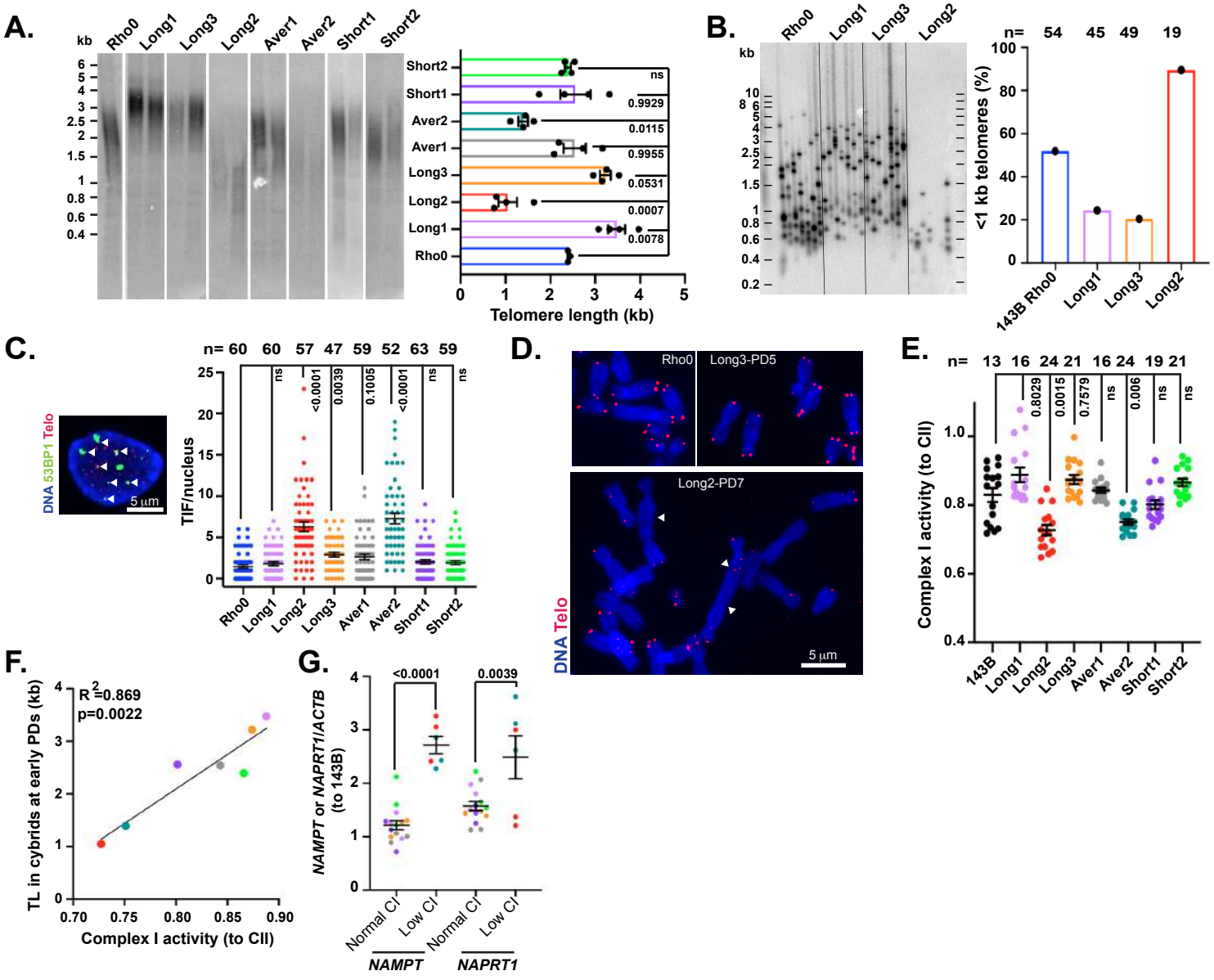

Figure 4

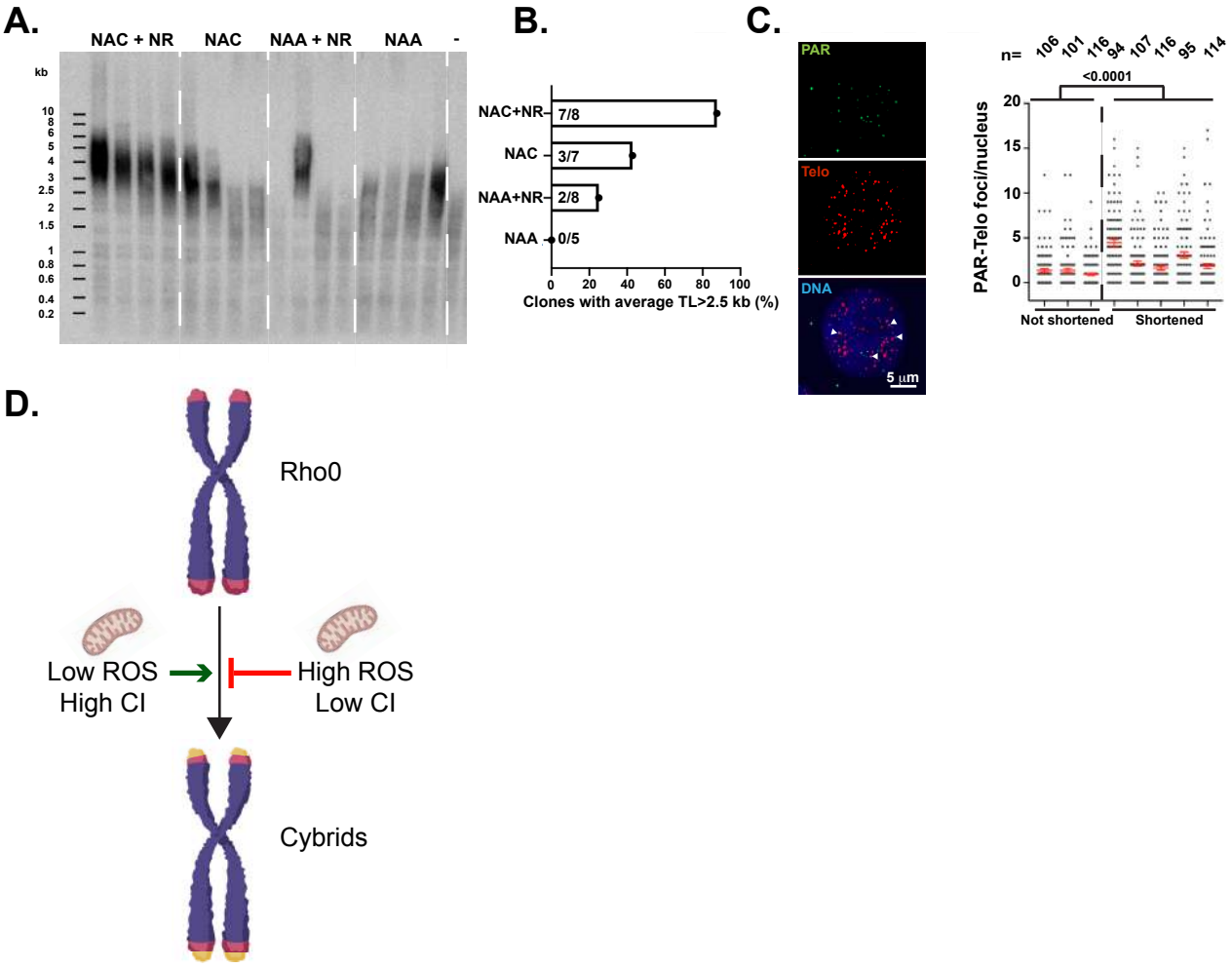

Figure 5

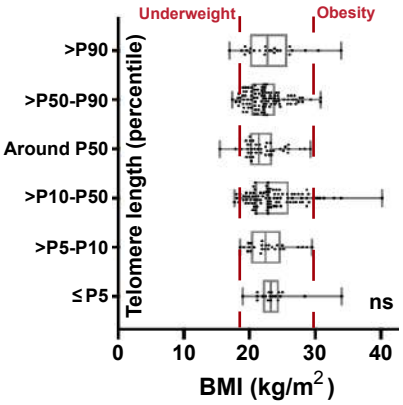

Figure S1

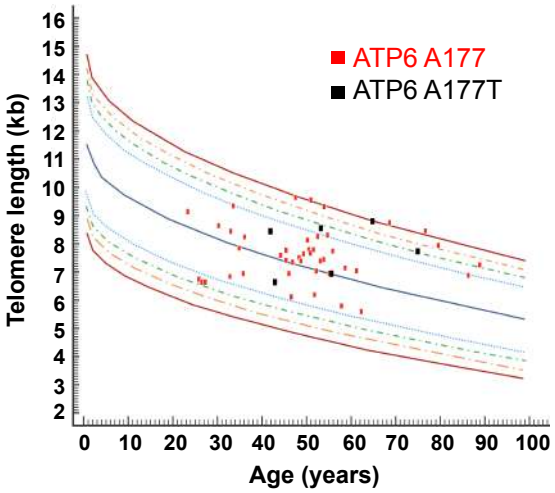

Figure S2

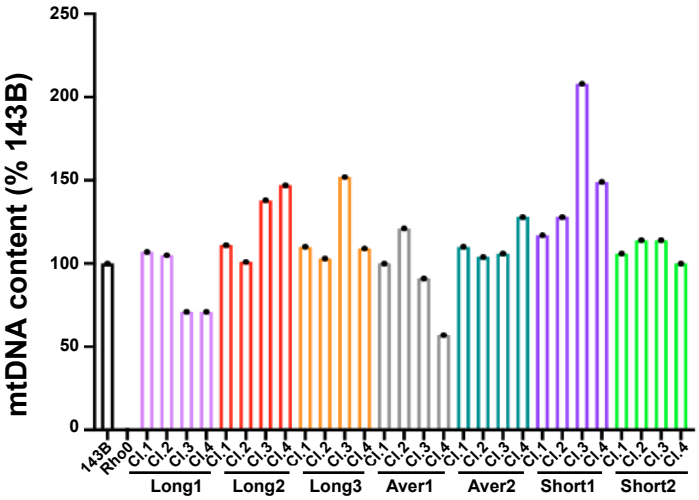

Figure S3

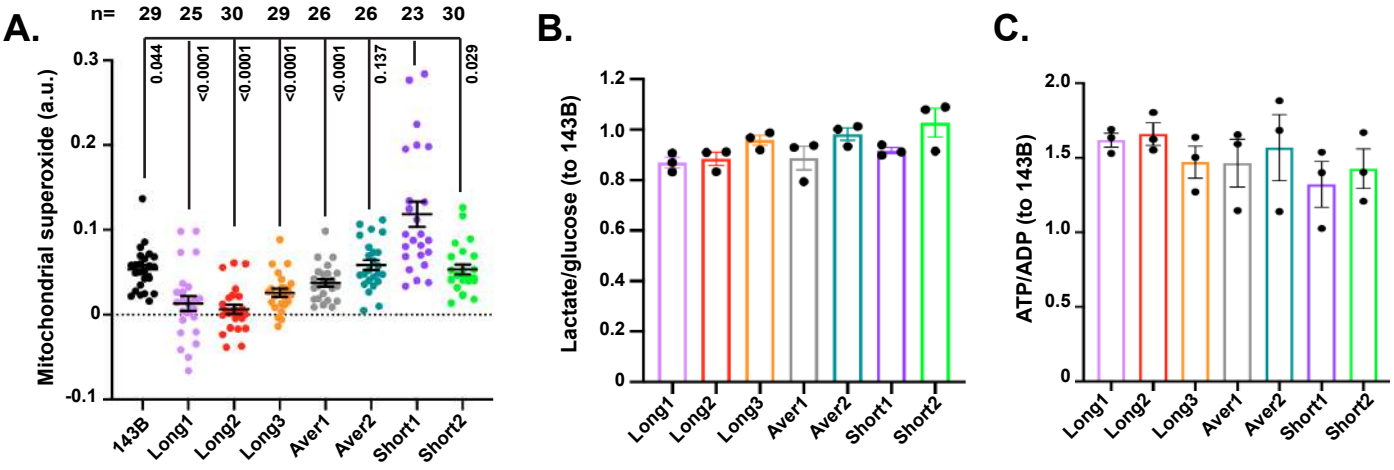

Figure S4

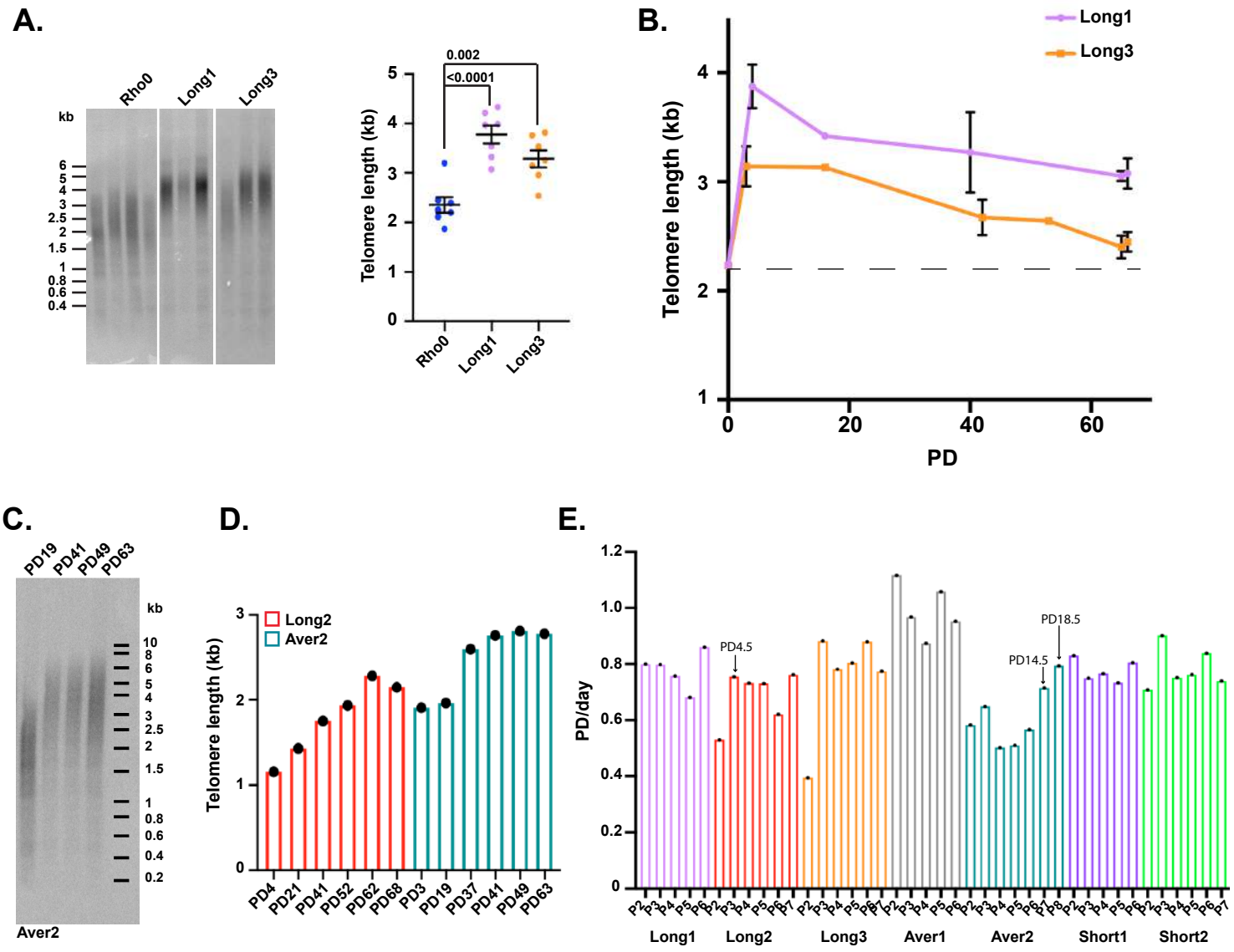

Figure S5

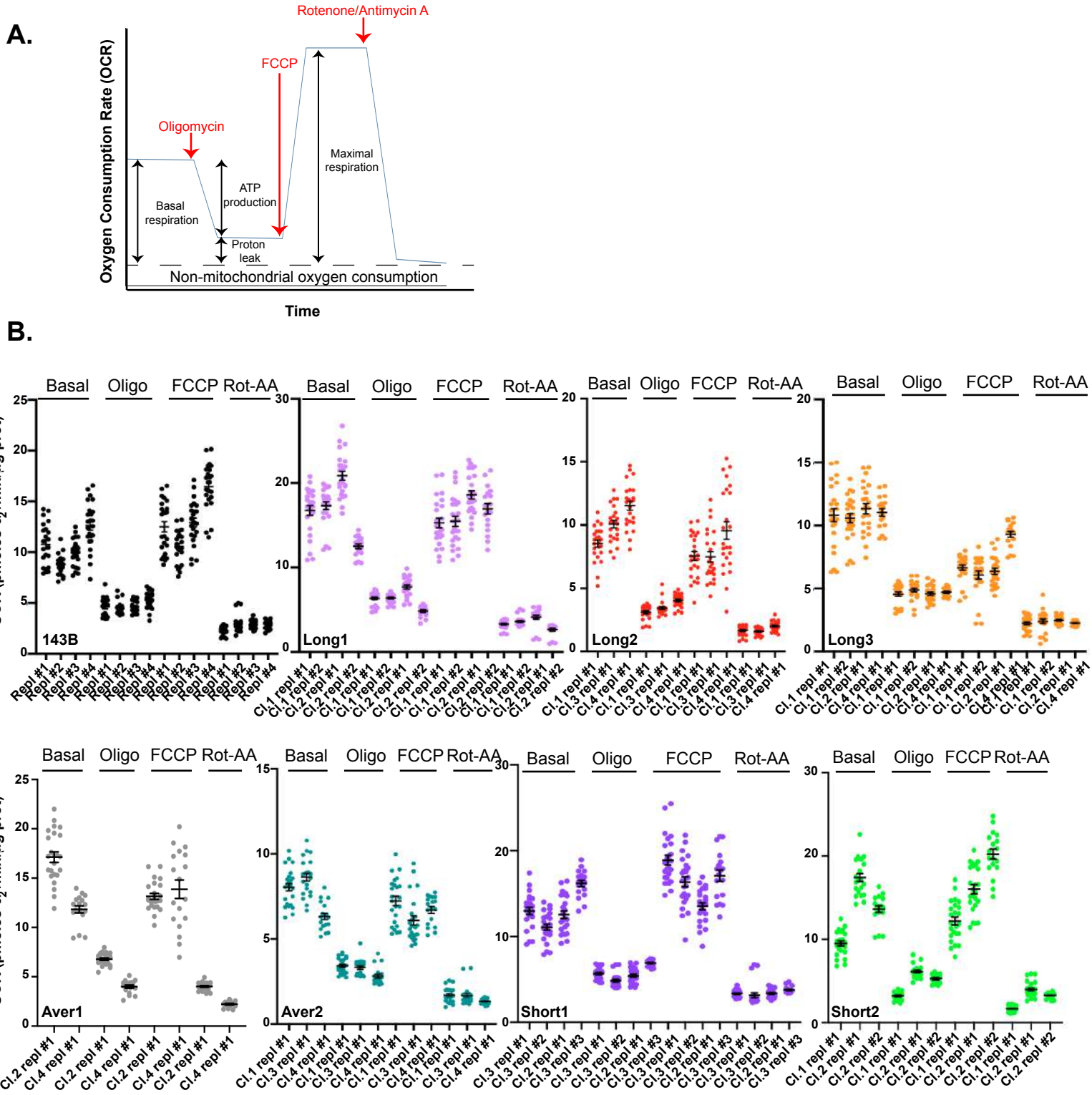

Figure S6

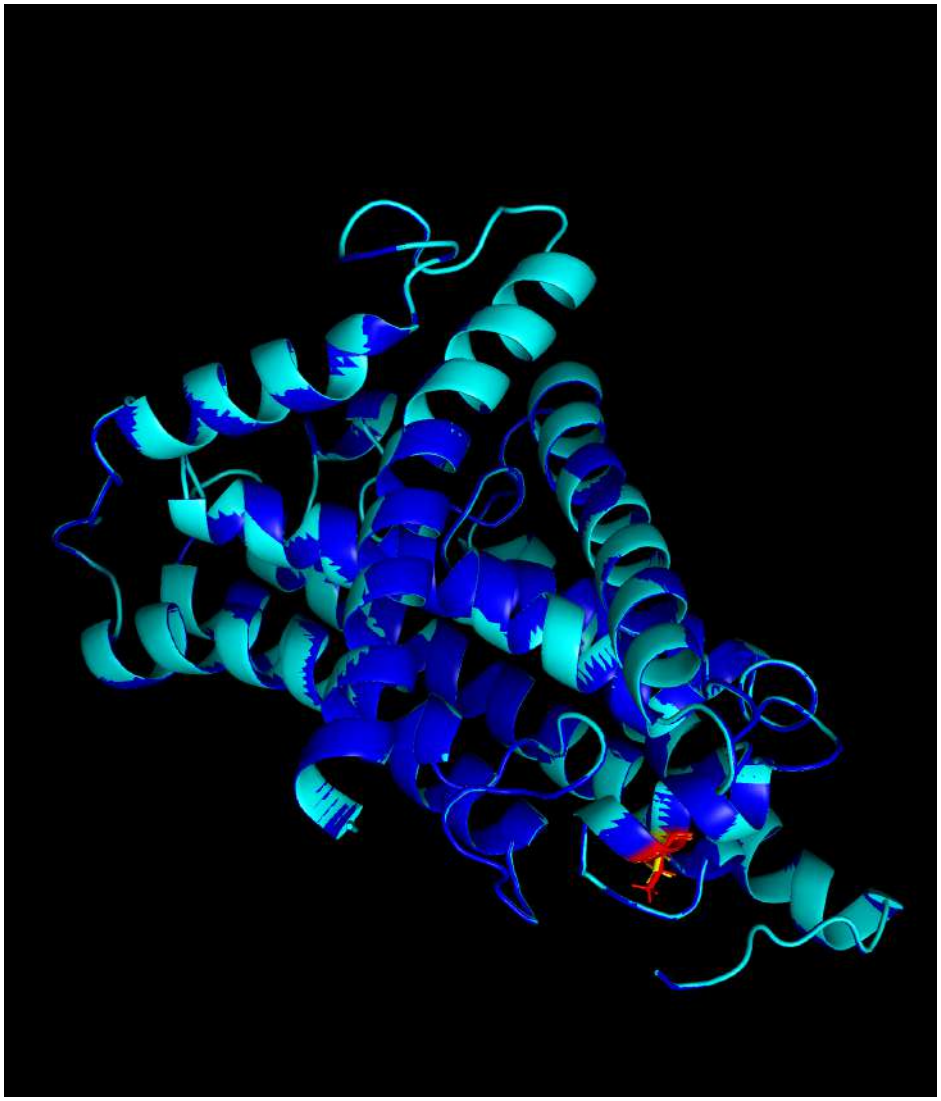

Figure S7

Table S1. Flow-FISH data.

Age (Years)	Lymphocytes (kb)	Granulocytes (kb)
0,02	10,40	9,44
0,07	12,09	11,05
0,09	12,29	10,97
0,10	10,44	9,27
0,18	10,96	9,85
0,30	8,94	7,35
0,36	9,65	8,50
0,50	10,68	9,54
0,67	12,49	11,22
0,76	11,06	9,77
0,85	12,93	12,98
0,88	11,77	9,91
0,94	12,04	11,05
1,02	11,88	11,26
1,13	9,89	9,40
1,36	10,89	9,96
1,41	10,78	9,55
1,60	9,95	9,06
1,62	9,91	9,17
1,66	12,82	11,44
1,66	9,73	9,11
1,78	9,66	8,87
1,82	9,90	9,05
1,83	9,72	8,17
1,87	11,11	10,69
1,90	12,19	10,79
1,99	12,53	11,86
2,02	8,45	7,70
2,07	13,02	11,93
2,09	12,60	11,98
2,15	13,26	12,02
2,21	10,79	9,14
2,22	10,57	9,45
2,32	11,69	10,58
2,52	11,37	10,60
2,57	11,04	8,64
2,60	8,75	7,84
2,64	9,81	8,81
2,80	8,97	8,17
2,83	12,99	12,11
2,93	9,83	9,42
3,03	11,14	11,76
3,06	11,82	10,81
3,15	9,56	8,75

3,17	10,69	9,21
3,18	9,84	9,28
3,22	9,91	9,14
3,47	10,57	11,05
3,51	11,77	11,05
3,52	11,28	10,87
3,55	12,37	11,01
3,59	12,18	11,35
3,66	8,44	8,43
3,67	12,16	11,29
3,77	9,28	7,82
3,84	10,04	9,50
4,03	9,96	9,06
4,05	11,57	11,47
4,06	11,52	9,93
4,47	10,85	11,56
4,48	9,71	8,81
4,52	10,53	9,28
4,56	9,95	9,29
4,75	11,02	10,88
5,00	11,43	10,93
5,02	9,55	10,17
5,04	12,50	11,21
5,04	9,34	9,23
5,16	9,53	7,62
5,17	13,01	12,36
5,43	8,71	8,59
5,43	9,21	7,91
5,44	8,53	7,67
5,52	8,69	8,40
5,53	10,66	9,62
5,57	9,72	9,02
5,71	9,63	9,17
5,74	12,42	12,03
5,75	9,46	8,88
5,77	8,41	7,77
5,78	9,23	8,97
5,79	11,18	11,25
5,82	7,79	7,47
6,06	10,79	9,73
6,19	8,11	8,36
6,19	9,76	8,87
6,94	8,30	8,67
6,95	11,91	11,32
6,96	10,42	9,93
6,98	9,68	8,97

7,41	9,12	9,07
7,44	10,06	9,69
7,69	10,21	9,53
7,91	9,13	8,59
8,39	9,53	9,55
8,44	8,82	8,21
8,51	9,66	8,90
8,55	8,32	8,76
8,66	9,87	9,07
8,68	10,95	10,40
8,82	11,19	11,11
8,86	9,99	10,43
8,87	7,12	6,19
9,26	9,61	10,06
9,31	8,78	9,13
9,49	11,78	10,88
9,67	8,93	9,22
9,78	9,26	8,83
9,83	8,57	8,67
9,86	10,06	9,37
10,08	9,79	8,76
10,08	8,39	7,74
10,10	10,35	10,61
10,12	10,06	9,27
10,24	8,44	7,59
10,27	11,15	9,91
10,27	9,05	8,93
10,30	8,93	9,23
10,69	11,49	10,60
10,88	10,19	9,35
10,88	8,72	8,18
10,93	9,34	10,08
11,08	10,42	9,74
11,11	8,53	8,52
11,17	11,60	10,88
11,21	9,52	9,81
11,26	7,53	7,85
11,39	12,49	12,63
11,53	12,08	11,62
11,54	8,22	8,22
11,57	10,28	10,60
11,63	12,23	11,57
11,73	9,38	8,18
11,75	10,82	11,16
11,75	8,35	7,45
12,03	8,98	8,57

12,30	9,12	9,12
12,32	9,26	8,88
12,35	10,58	10,00
12,35	8,72	8,79
12,37	8,32	8,31
12,48	9,83	8,97
12,48	7,97	7,56
12,59	8,34	7,41
12,82	9,87	9,59
13,07	9,60	9,26
13,08	10,45	9,52
13,13	9,61	9,18
13,20	9,10	8,73
13,34	11,08	11,67
13,48	9,47	8,45
13,52	11,86	11,15
13,58	10,60	10,47
13,77	9,63	8,97
13,85	9,27	9,11
13,86	9,07	7,91
13,92	8,73	8,70
13,99	9,28	9,64
14,11	9,74	9,73
14,40	10,27	10,41
14,47	8,37	8,62
14,48	9,27	9,00
14,70	10,41	9,71
14,77	9,55	9,35
15,02	8,56	8,26
15,11	8,74	7,93
15,26	11,19	10,83
15,48	11,85	11,24
15,53	9,95	9,04
15,94	10,42	9,23
16,28	9,84	9,84
16,71	9,41	9,71
16,72	10,23	10,63
16,79	10,25	9,37
17,20	8,91	7,96
17,52	8,51	8,74
17,65	9,48	8,62
17,73	11,09	11,18
17,77	9,24	8,82
17,78	9,11	8,24
17,90	7,63	9,38
17,92	9,05	8,40

18,21	8,69	8,88
18,30	9,97	10,59
18,90	9,23	9,10
19,70	7,28	8,78
19,90	8,92	10,22
20,10	8,29	9,75
20,40	6,54	7,57
20,40	5,85	7,64
20,53	10,07	10,39
20,60	7,30	7,65
20,84	9,08	9,70
21,00	8,67	9,57
21,12	10,64	11,24
21,16	9,58	11,05
21,35	8,97	9,24
21,35	9,51	9,96
21,43	10,56	11,58
21,60	7,76	9,82
21,85	9,85	10,29
21,93	10,84	11,45
22,10	9,50	9,75
22,10	10,77	11,27
22,18	7,21	8,36
22,19	8,51	9,45
22,30	7,91	9,01
22,88	9,24	8,48
22,90	10,89	10,18
23,09	8,18	8,33
23,10	10,96	11,29
23,10	8,08	9,60
23,30	7,08	7,03
23,40	8,63	8,03
23,50	8,05	8,08
23,68	7,68	8,40
23,86	9,50	9,46
24,10	10,61	9,74
24,22	8,84	8,50
24,50	6,91	7,05
24,50	7,57	7,71
24,60	8,60	8,32
24,90	9,52	9,74
25,00	7,55	7,08
25,00	7,70	6,98
25,20	9,31	9,69
25,30	6,81	6,29
25,33	9,32	8,53

25,33	8,14	8,25
25,50	7,26	7,51
25,54	8,66	8,81
25,60	7,97	8,24
25,60	8,39	9,28
25,60	6,40	7,14
25,70	9,38	8,17
25,80	8,25	8,08
25,80	7,06	6,76
25,80	9,11	9,33
25,90	8,12	8,18
25,90	6,54	6,53
25,90	8,53	8,71
26,00	6,21	6,90
26,10	8,30	8,21
26,10	9,49	9,14
26,30	6,50	6,72
26,30	6,72	7,42
26,40	6,12	6,71
26,40	8,05	7,67
26,50	8,11	8,54
26,50	8,41	8,69
26,90	9,15	8,38
26,93	6,19	6,93
27,10	6,93	7,39
27,20	9,03	8,45
27,30	9,48	8,44
27,59	8,02	7,58
27,70	7,17	6,93
27,70	5,99	6,27
27,80	7,22	7,79
27,80	6,89	6,70
27,90	8,37	8,20
28,00	7,17	7,14
28,10	8,80	9,59
28,10	8,87	8,84
28,23	8,73	7,47
28,30	6,47	6,44
28,44	6,37	7,40
28,50	7,14	7,94
28,50	8,40	8,90
28,68	8,80	7,84
28,70	8,31	9,07
28,80	8,25	8,52
28,80	9,09	9,20
28,80	7,38	6,68

28,80	8,22	7,23
28,85	7,33	8,60
29,00	9,22	9,73
29,16	8,17	7,92
29,40	8,81	9,23
29,42	9,58	10,74
29,64	6,53	7,38
29,65	7,54	8,12
29,72	8,79	7,83
29,78	8,58	8,59
29,89	7,40	7,52
29,97	7,17	6,54
30,00	8,23	9,17
30,07	8,57	8,18
30,09	8,06	9,19
30,14	8,14	8,03
30,26	9,58	10,11
30,42	8,24	8,12
30,54	8,17	8,17
30,61	9,55	9,96
30,87	7,26	6,94
31,15	7,96	7,12
31,18	8,48	8,38
31,26	8,48	8,48
31,36	6,16	6,54
31,60	8,68	8,19
31,64	7,74	7,64
31,75	6,69	6,89
31,77	8,48	9,19
32,09	7,00	7,22
32,10	7,23	7,28
32,27	6,77	6,90
32,33	8,45	8,38
32,47	6,74	6,72
32,69	8,77	8,30
32,71	9,25	9,51
32,98	8,53	8,31
33,11	9,41	9,93
33,12	5,92	6,02
33,29	7,66	7,09
33,42	7,71	7,46
33,44	7,70	7,27
33,57	8,54	8,46
33,60	7,07	6,95
33,65	6,46	6,67
34,08	6,49	5,92

34,29	6,51	6,69
34,31	7,89	8,18
34,34	9,02	9,32
34,44	8,57	8,83
34,53	7,09	6,61
34,77	9,44	9,27
35,17	8,67	8,95
35,30	7,04	6,84
35,74	8,43	7,87
35,77	7,65	7,96
35,78	8,09	7,56
35,97	8,63	7,81
36,08	7,36	6,80
36,22	8,30	7,37
36,28	7,91	7,16
36,70	6,56	7,48
37,13	6,06	6,70
37,18	8,24	7,25
37,33	8,32	7,75
37,42	7,84	7,45
37,43	6,71	6,53
37,47	7,41	7,04
37,51	8,37	8,38
37,97	8,04	8,23
38,37	5,54	5,86
38,68	6,11	6,66
39,54	7,31	6,91
39,55	8,39	8,78
40,51	8,70	8,55
40,53	6,20	6,55
40,75	7,40	7,10
40,85	7,99	7,87
40,87	6,92	7,83
41,14	6,77	6,46
41,22	8,28	7,82
41,31	8,51	8,20
42,21	6,71	7,65
42,58	7,54	7,95
42,98	6,35	6,29
43,04	7,45	7,27
43,06	8,91	8,47
43,61	7,90	7,56
43,64	7,72	7,31
43,75	7,42	7,55
43,86	8,55	7,47
44,47	6,18	6,91

44,80	7,52	7,86
44,87	7,29	7,28
44,89	7,76	8,05
45,50	7,05	7,06
45,51	8,26	7,93
46,03	8,38	8,48
46,17	6,16	6,35
46,44	7,44	7,98
46,77	9,68	9,62
47,33	6,88	7,41
47,43	6,24	6,78
47,55	8,14	7,89
47,77	8,17	8,73
47,78	8,36	9,43
47,87	7,56	7,90
47,93	7,45	7,44
47,93	7,76	7,96
47,97	6,46	6,34
48,04	6,08	6,62
48,27	8,36	9,17
48,43	8,31	8,26
48,44	7,42	7,97
48,78	6,97	6,93
48,99	7,70	7,95
49,39	8,69	8,11
49,54	8,60	8,00
49,78	8,19	8,38
50,28	7,80	7,61
50,31	7,71	9,11
50,51	9,57	8,96
50,56	7,59	8,02
50,93	7,64	7,67
51,18	6,32	6,83
51,20	7,89	8,12
51,29	5,70	6,37
51,48	7,13	7,31
51,51	8,02	8,52
51,78	8,34	8,64
52,52	7,39	7,35
52,61	8,58	9,45
52,85	8,40	9,17
53,08	5,72	6,27
53,36	7,52	8,25
53,36	9,40	9,41
53,63	8,86	8,81
53,69	7,35	7,27

53,70	6,64	7,47
53,73	6,08	5,99
53,86	5,55	6,50
54,43	7,52	8,79
54,60	7,03	7,81
54,65	6,20	6,67
54,93	6,88	7,71
55,03	5,31	6,61
55,04	6,24	8,05
55,39	7,82	7,44
55,42	6,14	6,64
55,44	8,73	8,88
56,26	7,00	8,09
56,37	6,72	7,31
56,58	7,67	7,34
57,11	7,96	8,91
57,17	6,09	6,32
57,35	5,90	7,41
57,69	7,43	7,01
58,23	7,24	7,26
58,77	7,41	8,30
58,86	6,48	8,75
58,90	7,80	7,35
59,13	8,09	7,37
59,44	8,10	8,17
59,61	6,21	7,34
59,68	5,95	7,33
59,78	6,70	8,30
59,87	5,34	5,57
60,61	6,88	8,59
61,13	8,56	8,91
61,52	5,00	6,59
61,61	8,17	9,51
61,68	6,30	7,19
61,69	5,66	6,63
61,93	5,59	6,76
62,11	5,67	5,89
62,18	6,37	6,65
62,19	7,54	8,37
62,80	7,10	7,34
62,34	8,60	7,69
63,03	6,44	6,91
63,48	6,65	7,25
63,61	6,25	6,50
63,76	5,71	6,38
64,00	6,72	7,94

64,68	6,80	7,01
64,79	5,89	6,53
65,32	5,98	6,46
66,03	8,55	8,75
67,53	7,11	8,52
68,19	8,32	9,15
68,40	6,98	7,72
68,65	5,71	6,66
68,69	5,20	6,84
69,40	6,35	7,07
70,01	5,63	7,03
70,78	5,73	5,85
70,94	6,76	7,85
71,60	6,87	6,89
72,53	6,10	6,67
73,01	6,99	7,12
74,27	4,91	5,93
74,76	4,49	5,33
75,69	7,24	7,28
76,69	7,71	8,73
78,03	5,97	7,12
78,03	6,78	6,88
79,65	4,69	5,91
81,63	6,63	7,86
81,94	5,70	7,56
82,69	5,24	5,99
83,18	6,21	7,32
84,30	4,52	6,21
84,94	6,24	7,33
84,99	6,95	8,11
86,03	3,98	5,47
90,69	5,00	5,72
99,18	4,56	6,09

Table S2. Primers used in this study.

	Primer	Sequence
mtDNA sequencing	mt-R1	ACT-CCA-CCA-TTA-GCA-CCC-AAA-GC
	mt-R30	TGG-AGA-GCT-CCC-GTG-AGT-GGT-T
	mt-R2	CAT-AAA-GCC-TAA-ATA-GCC-CAC-ACG
	mt-R31	GGT-GAT-GTG-AGC-CCG-TCT-AAA-C
	mt-R3	ACA-CCG-CTG-CTA-ACC-CCA-TAC
	mt-R32	AGT-GTT-CTG-GCG-AGC-AGT-TTT-G
	mt-R4	AGC-TAA-GAC-CCA-AAC-TGG-GAT-T
	mt-R33	GGT-TTA-GCT-CAG-AGC-GGT-CAA-G
	mt-R5	AGT-GCA-CTT-GGA-CGA-ACC-AGA-G
	mt-R17	TGT-GAG-GAG-TTC-AGT-TAT-AT
	mt-R6	CAA-AGA-GGA-ACA-GCT-CTT-TGG-A
	mt-R34	GGG-TCT-TCT-CGT-CTT-GCT-GTG-T
	mt-R7	ACC-TGT-ATG-AAT-GGC-TCC-AC
	mt-R35	GGC-TCT-GCC-ATC-TTA-ACA-AAC-C
	mt-R8	GAG-AAA-TAA-GGC-CTA-CTT-CAC-AAA-GC
	mt-R36	CTA-GGA-AGA-TTG-TAG-TGG-TGA-GGG-TG
	mt-R9	GAA-CTA-GTC-TCA-GGC-TTC-AAC-ATC-G
	mt-R37	TGC-CTT-GGG-TAA-CCT-CTG-GGA-CTC
	mt-R10	CGG-ACA-ATG-AAC-CAT-AAC-CAA-TAC-TA
	mt-R38	TTG-CGT-TCA-GTT-GAT-GCA-GAG-TGG
	mt-R11	CCT-TAC-CAC-GCT-ACT-CCT-ACC-TAT-CTC-C
	mt-R39	CTC-CAG-CTC-ATG-CGC-CGA-ATA-ATA-G
	mt-R12	CAA-TTC-AAT-ATG-AAA-ATC-ACC-TCG-G
	mt-R40	TAG-GAC-TGC-TGT-GAT-TAG-GAC-GG
	mt-R13	CTT-AGG-GGC-CAT-CAA-TTT-CAT-CAC
	mt-R41	TGG-ATT-TTG-GCG-TAG-GTT-TGG-TCT
	mt-R14	CCC-ACT-TCC-ACT-ATG-TCC-TAT-CAA-T
	mt-R42	GGA-AAA-TGA-TTA-TGA-GGG-CGT-GAT
	mt-R15	CAC-ATT-CGA-AGA-ACC-CGT-ATA-CAT-AAA
	mt-R43	CGG-TAG-TAT-TTA-GTT-GGG-GCA-TTT-CAC
	mt-R16	CCA-CAG-TTT-CAT-GCC-CAT-CGT-CC
	mt-R44	GAT-AGG-CAT-GTG-ATT-GGT-GGG
	mt-R18	CTG-TCG-CCT-TAA-TCC-AAG-CCT-ACG
	mt-R45	GAA-TGT-TGT-CAA-AAC-TAG-TTA-ATT-GGA-AGT
	mt-R19	GCC-TGA-TAC-TGG-CAT-TTT-GT
	mt-R46	GGC-GGC-AAA-GAC-TAG-TAT-GG
	mt-R20	CAC-CTC-ATA-TCC-TCC-CTA-CTA-TGC
	mt-R47	TTC-TTG-GGC-AGT-GAG-AGT-GA
	mt-R21	GCT-CCC-TTC-CCC-TAC-TCA-TC
	mt-R48	CCC-CAT-TGT-GTT-GTG-GTA-AA
	mt-R22	CAC-GTT-CTC-CTG-ATC-AAA-TAT-CAC
	mt-R49	GAA-GAA-CTG-ATT-AAT-GTT-TGG-GTC-T
	mt-R23	TCA-TCC-CTG-TAG-CAT-TGT-TCG
	mt-R50	GTG-GTG-ATA-GCG-CCT-AAG-CA
	mt-R24	CTT-CCA-CCC-CCT-AGC-AGA-A
	mt-R51	GGG-TGG-GGT-TAT-TTT-CGT-TAA-TGT

	mt-R25	TCG-CTA-CCT-CCC-TGA-CAA-GC
	mt-R52	GAG-ATT-GCT-CGG-GGG-AAT-AG
	mt-R26	CCT-CAA-CCC-AAA-AAG-GCA-TAA
	mt-R53	GGT-TGT-AGT-CCG-TGC-GAG-AA
	mt-R27	CCC-CCA-TAA-ATA-GGA-GAA-GGC-TTA
	mt-R54	ACT-GTG-GCC-CCT-CAG-AAT-GA
	mt-R28	CCT-GAA-ACA-TCG-GCA-TTA-TCC
	mt-R55	CAA-GGA-CGC-CTC-CTA-GTT-TG
	mt-R29	CCA-CAT-CAA-GCC-CGA-ATG-A
	mt-R56	CGG-TTG-TTG-ATG-GGT-GAG-T
mtDNA qPCR	mt-R11	CCT-TAC-CAC-GCT-ACT-CCT-ACC-TAT-CTC-C
	mt-R39	CTC-CAG-CTC-ATG-CGC-CGA-ATA-ATA-G
hTR qPCR	hTR-1	TTG-CTC-TAG-AAT-GAA-CGG-TGG-A
	hTR-2	TTT-GTC-TAA-CCC-TAA-CTG-AGA-AG
NAMPT qRT-PCR	NAMPT-F	TCA-AGA-AGT-ACA-CAG-GCA-CCA
	NAMPT-R	GTG-GCA-GCA-ACT-TGT-AAC-CC
NAPRT1 qRT-PCR	NAPRT1-F	CAT-TGG-CAC-CAG-TGT-GGT-CA
	NAPRT1-R	TCC-TCG-GTC-AGC-TTC-ATT-CG
ACTB qRT-PCR	ACTB-F	TGT-ACG-CCA-ACA-CAG-TGC-TG
	ACTB-R	GCT-GGA-AGG-TGG-ACA-GCG-A
TeSLA	TeSLA-T 1	ACT-GGC-CAC-GTG-TTT-TGA-TCG-ACC-CTA-AC
	TeSLA-T 2	ACT-GGC-CAC-GTG-TTT-TGA-TCG-ATA-ACC-CT
	TeSLA-T 3	ACT-GGC-CAC-GTG-TTT-TGA-TCG-ACC-TAA-CC
	TeSLA-T 4	ACT-GGC-CAC-GTG-TTT-TGA-TCG-ACT-AAC-CC
	TeSLA-T 5	ACT-GGC-CAC-GTG-TTT-TGA-TCG-AAA-CCT-TA
	TeSLA-T 6	ACT-GGC-CAC-GTG-TTT-TGA-TCG-AAC-CCT-AA
	TeSLAADR1C3S	GGT-TAC-TTT-GTA-AGC-CTG-TC
	Adapter	TGT-AGC-GTG-AAG-ACG-ACA-GAA
	TeSLA TP	TGG-CCA-CGT-GTT-TTG-ATC-GA
	TeSLA P22 TA	TAG-ACA-GGC-TTA-CAA-AGT-AAC-CAT-GGT-GGA-GAA-TTC-TGT-CGT-CTT-CAC-GCT-ACA-TT
	TeSLA P22 AT	ATG-ACA-GGC-TTA-CAA-AGT-AAC-CAT-GGT-GGA-GAA-TTC-TGT-CGT-CTT-CAC-GCT-ACA-TT
Mycoplasma qPCR	Myco-F	GGC-GAA-TGG-GTG-AGT-AAC-ACG
	Myco-R	CGG-ATA-ACG-CTT-GCG-ACC-TAT-G